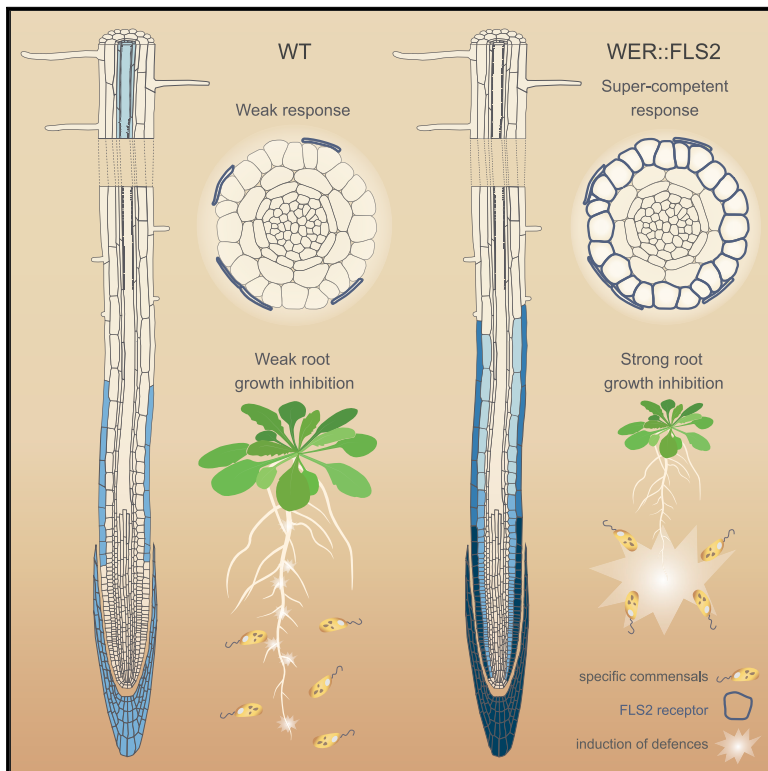


# Current Biology

## Spatially Restricted Immune Responses Are Required for Maintaining Root Meristematic Activity upon Detection of Bacteria

### Graphical Abstract



### Authors

Aurélia Emonet, Feng Zhou,  
Jordan Vacheron, ...,  
Paul Schulze-Lefert, Christoph Keel,  
Niko Geldner

### Correspondence

niko.geldner@unil.ch

### In Brief

By installing immune responsiveness specifically in peripheral root meristem cells, Emonet et al. generate hyperresponsive plants, showing flagellin-dependent root collapse and growth inhibition by commensal bacteria. This highlights the relevance of spatially resolved immune responses and their importance for bacterial accommodation by roots.

### Highlights

- Cell-specific expression of an immune receptor reveals general and specific responses
- Immune signaling appears to separate into autonomous and non-autonomous branches
- Immune response in some meristem cells causes meristem collapse and growth arrest
- Mis-localized immune perception interferes with accommodation of commensal bacteria

Article

# Spatially Restricted Immune Responses Are Required for Maintaining Root Meristematic Activity upon Detection of Bacteria

Aurélia Emonet,<sup>1</sup> Feng Zhou,<sup>1,4</sup> Jordan Vacheron,<sup>2</sup> Clara Margot Heiman,<sup>2</sup> Valérie Dénervaud Tendon,<sup>1</sup> Ka-Wai Ma,<sup>3</sup> Paul Schulze-Lefert,<sup>3</sup> Christoph Keel,<sup>2</sup> and Niko Geldner<sup>1,5,6,\*</sup>

<sup>1</sup>Department of Plant Molecular Biology, University of Lausanne, Biophore, UNIL-Sorge, 1015 Lausanne, Switzerland

<sup>2</sup>Department of Fundamental Microbiology, University of Lausanne, Biophore, UNIL-Sorge, 1015 Lausanne, Switzerland

<sup>3</sup>Department of Plant Microbe Interactions, Max Planck Institute for Plant Breeding Research, Carl-von-Linné-Weg 10, 50829 Cologne, Germany

<sup>4</sup>Present address: National Key Laboratory of Plant Molecular Genetics, CAS Center for Excellence in Molecular Plant Sciences, Chinese Academy of Sciences, 300 Feng Lin Road, Shanghai 200032, China

<sup>5</sup>Twitter: @NikoGeldner

<sup>6</sup>Lead Contact

\*Correspondence: [niko.geldner@unil.ch](mailto:niko.geldner@unil.ch)

<https://doi.org/10.1016/j.cub.2020.12.048>

## SUMMARY

Plants restrict immune responses to vulnerable root parts. Spatially restricted responses are thought to be necessary to avoid constitutive responses to rhizosphere microbiota. To directly demonstrate the importance of spatially restricted responses, we expressed the plant flagellin receptor (FLS2) in different tissues, combined with fluorescent defense markers for immune readouts at cellular resolution. Our analysis distinguishes responses appearing cell autonomous from apparently non-cell-autonomous responses. It reveals lignification as a general immune response, contrasting suberization. Importantly, our analysis divides the root meristem into a central zone refractory to FLS2 expression and a cortex that is sensitized by FLS2 expression, causing meristem collapse upon stimulation. Meristematic epidermal expression generates super-competent lines that detect native bacterial flagellin and bypass the weak or absent response to commensals, providing a powerful tool for studying root immunity. Our manipulations and readouts demonstrate incompatibility of meristematic activity and defense and the importance of cell-resolved studies of plant immune responses.

## INTRODUCTION

Similar to the intestinal microbiome of animals, plant roots host a vast range of micro-organisms in their rhizosphere. Among those, some can act as pathogens, negatively impacting growth and reproduction. In both animals and plants, a sophisticated immune system keeps the vast majority of pathogens at bay, while allowing colonization with commensal and beneficial microbes.<sup>1,2</sup> In plants, this immunity rests on the recognition of highly conserved microbe-associated molecular patterns (MAMPs), recognized by an extended set of plasma-membrane-localized pattern-recognition receptors (PRRs).<sup>3</sup> One of the most investigated MAMPs is a 22-amino-acid fragment of the bacterial flagellin protein (flg22). It is detected by the FLAGELLIN SENSING 2 (FLS2) receptor<sup>4–7</sup> and induces a signaling cascade, including reactive oxygen species (ROS) production, calcium signaling, MAPKs (mitogen-activated protein kinase) phosphorylation, and gene transcription, eventually leading to defense responses, such as callose and lignin deposition or phytoalexin production.<sup>8,9</sup>

Yet plant PRRs equally perceive MAMPs from commensal or beneficial microbes, which are part of the normal plant rhizosphere. Whereas MAMP-triggered immunity (MTI) is associated

with growth inhibition,<sup>5,10</sup> a plethora of publications have established a growth-promoting action of the soil microbiome.<sup>11</sup> It is therefore of particular interest to understand how roots accommodate a rhizosphere community, while avoiding a constant activation of PRRs and the growth-defense trade-off that comes with it. Many researchers have argued that growth inhibition can be overcome by the ability of commensal micro-organisms to suppress plant immunity.<sup>12</sup> In addition, it was recently shown that the root has an inherently dampened MAMP response until it encounters damage, which locally boosts immune responsiveness.<sup>13</sup>

Indeed, root immune responses are often lower than in the shoot, in part because of an absence or low abundance of PRRs.<sup>14–16</sup> Moreover, plants restrict their defense to regions considered vulnerable, such as regions with absent or broken endodermal barriers, such as the elongation zone or lateral root emergence sites. It is also there where bacteria are found to preferentially accumulate.<sup>13–15,17–20</sup>

Here, we set out to address the relevance of spatially limited immune responses. Wyrsh et al.<sup>21</sup> ectopically expressed FLS2 under tissue-specific promoters, and their data suggested that all root tissues were competent to mount an immune

response provided that *FLS2* is expressed, although the nature of the tissue had a large influence on the strength of the innate immune responses. Yet the immune readouts used were at whole-plant or organ-level resolution and did not allow the authors to conclude from which cell type responses were originating and whether they were cell autonomous, regional, or systemic. MAMPs induce ROS production, as well as cytosolic calcium increases, both of which are known to act in paracrine, even systemic signaling.<sup>22–25</sup> Indeed, calcium waves were reported to initiate in the root elongation zone and to spread across tissues after flg22 treatment,<sup>26,27</sup> opening the possibility that MAMP responses could be induced in cell layers far away from the site of MAMP perception.

By adding cellular resolution reporters to these cell-type-specific *FLS2* expression lines, we were able to both manipulate and quantitatively map defense responses at cellular resolution in the root. Our approach reveals the presence of regions refractory to *FLS2* presence, as well as others which are super-competent. We show that restricted *FLS2* expression in meristematic epidermis has drastic impact on root development, affecting growth, cell wall composition, and cell viability. To assess the impact of *FLS2* misexpression in response to natural microbiota, we use our super-competent lines in the presence of commensal bacteria that are not or only weakly inducing responses in wild-type (WT) plants. We demonstrate stimulation of *FLS2* directly by native, bacteria-derived flagellin and reveal the importance of spatial restriction of immune responses in order to adequately balance growth and defense.

## RESULTS

In order to obtain cellular resolution readouts of immune responses in the different *FLS2*-expressing lines, we combined them with a set of fluorescent transcriptional response markers. These marker lines use a triple mVenus fluorochrome coupled to a nuclear localization signal (*prom::NLS-3xmVenus*). Combining concatemerization with nuclear concentration generates high sensitivity and allows for a clear cellular assignment, not achievable with cytosolic, endoplasmic reticulum (ER), or plasma-membrane-localized markers. These lines now enable us to observe damage and defense responses with cellular resolution, adding a crucial layer of complexity to our analyses of damage and immune responses.<sup>13,20,25,28</sup> In addition to these transcriptional reporter lines, we also employed fluorescence-based markers for cytosolic calcium changes triggered by flg22.<sup>29</sup>

### Tissue-Restricted Expression of the *FLS2* Receptor in *fls2* Mutants

In order to analyze the ability of the different root tissues to respond to flg22, we used lines expressing *FLS2* under cell-type-specific promoters in an *fls2* (SAIL691\_C04) mutant background.<sup>21</sup> We selected lines expressing *FLS2-GFP* driven by three different tissue-specific promoters: *WEREWOLF* for epidermis (*WER::FLS2*); *CASPARIAN STRIP DOMAIN PROTEIN 1* for endodermis (*CASP1::FLS2*); and *SHORT-ROOT* for inner cell layers (*SHR::FLS2*). As controls, we monitored *FLS2-GFP* driven by the constitutive promoter *UBIQUITIN 10* (*UBQ10::FLS2*) and by the native *FLS2* promoter (*FLS2::FLS2* in *Ws-0*). As described previously, endogenous *FLS2* expression was observed principally in

the differentiated stele<sup>14</sup> (Figure 1Ai) but also weakly in all tissues from the elongation to the differentiation zone, as well as in root cap cells (Figure 1Bi).<sup>13</sup> *WER::FLS2*, by contrast, was strongly expressed in the epidermis of the meristematic zone (Figures 1Aii and 1Bii), as predicted,<sup>30</sup> with some weak signal in the elongating cortex (Figure S1A). *CASP1::FLS2* had the predicted exclusive expression in differentiated endodermis (Figures 1Aiii, 1Biii, and S1B). In agreement with its established expression,<sup>31,32</sup> we detected *SHR::FLS2* in the stele close to the meristem (Figures 1Aiv and 1Biv) but also faintly in the neighboring endodermis, suggesting that either *FLS2* proteins or mRNAs move through plasmodesmata or that the *SHR* promoter has a low, overlooked activity in the endodermis (Figure S1D). *UBQ10::FLS2* was detected in all tissues throughout the root, from meristem to differentiation zone (Figures 1Av, 1Bv, and S1C).

### Quantitative Analysis of MAMP Response Patterns at Cellular Resolution

We then crossed our selection of *promoter::FLS2* lines with two lines expressing transcriptional markers of defense, *PER5::NLS-3xmVenus* (*PEROXIDASE 5*) and *MYB51::NLS-3xmVenus* (*MYB DOMAIN PROTEIN 51*), and generated homozygous lines at all three loci (marker, *prom::FLS2*, and *fls2* [SAIL691\_C04]). As a control, we used the same two markers in WT Col-0 background. Markers were chosen for their strong response to flg22 and their distinct response patterns.<sup>13,20,21</sup> In addition, we developed a pipeline using tissue-specific quantitative analysis for measuring and comparing MAMP responses in an unbiased fashion (Figure S2). For this, we additionally introduced ubiquitous nuclear markers (*UBQ10::NLS-mTurquoise2* or *UBQ10::NLS-tdTomato*) in all our genotypes, which allows to call all nuclei as separate, individual 3D regions of interests (ROIs), even those with weak or undetectable MAMP response. After mock or flg22 treatment and fixation, cell-wall-stained roots were imaged at three different zones of the root: meristem (MZ); elongation (EZ); and differentiation (DZ). Each nucleus was automatically detected as a 3D object, and the obtained nuclei object maps were then combined to the cell wall marker channels to manually curate and assign each nucleus to a tissue. Once the selected nuclei were assigned, mean intensity for each cell type per zone per treatment per genotype were calculated and color coded for the generation of a quantitative MAMP-response atlas for each *prom::FLS2* line (Figure S2; values in Figure S3).

### Ectopic *FLS2* Expression Alters MAMP Response Patterns

Our cell-specific quantification and microscopic analysis in *PER5*-expressing WT plants confirmed that *PER5* is not expressed in absence of flg22 treatment (Figures 2A–2C) but that *MYB51* presents a constitutive, flg22-independent expression in the epidermis and root cap cells of the undifferentiated tissues (MZ and EZ) and in the stele and the cortex of the DZ (Figures 3A and 3C). Both MAMP markers are strongly induced by flg22 in the EZ, recapitulating previous observations (Figures 2A and 3A).<sup>13,19,20</sup> Specifically, *PER5* is induced almost exclusively in the elongating epidermis and root cap cells (Figures 2C and 2D). Strong response in these tissues might be enhanced by feedforward regulation of flg22 on the endogenous *FLS2* promoter.<sup>13</sup> *MYB51* induction is restricted to these same tissues close to the

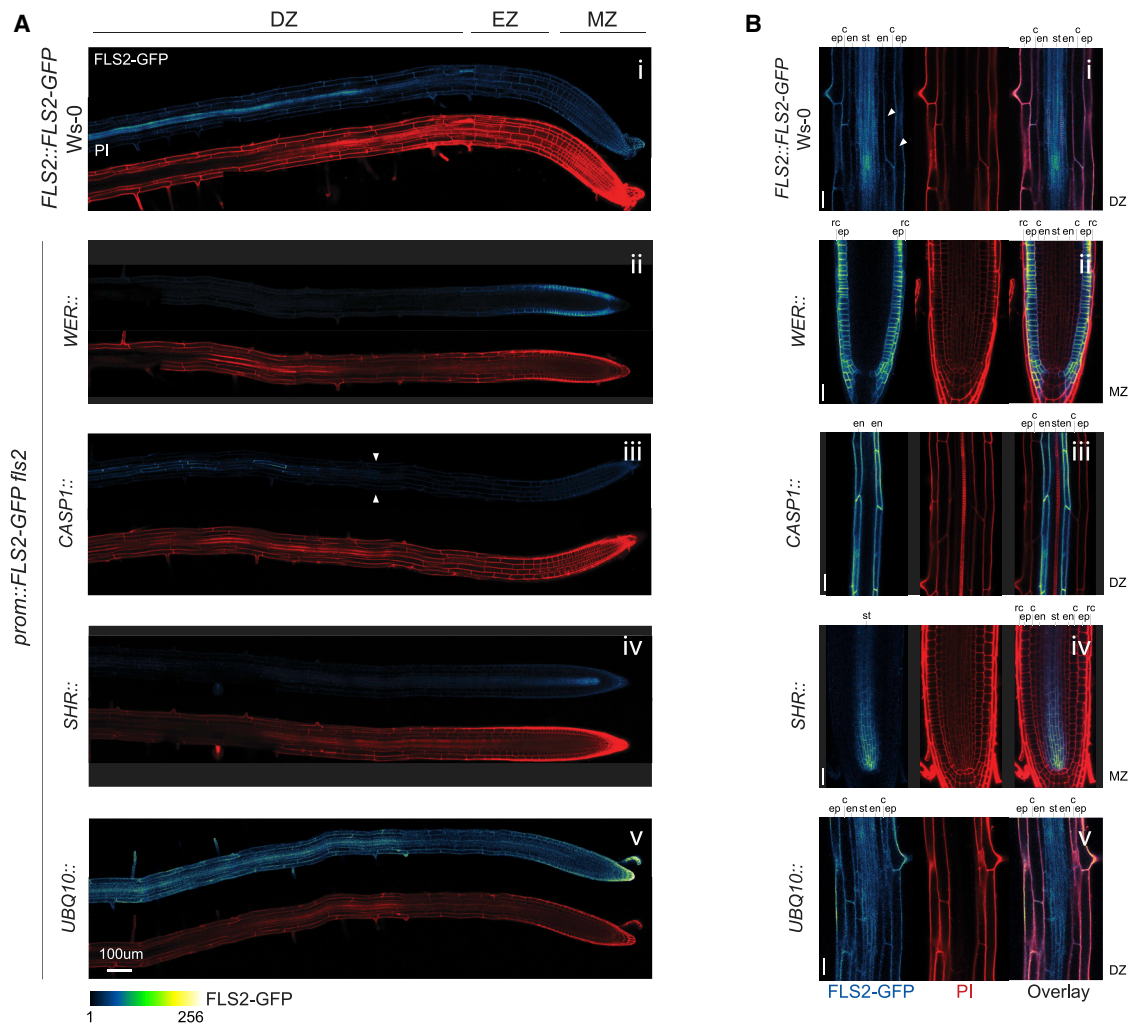


**Figure 1. Tissue-Specific Promoters Drive FLS2 Receptor Expression Ectopically**

(A) Tile scan of *fls2* (SAIL691\_C04) roots Col-0 background complemented with GFP-tagged FLS2 receptor under epidermal (*WER*::; ii), endodermal (*CASP1*::; iii), central cylinder (*SHR*::; iv), and ubiquitous (*UBQ10*::) promoters (v). For comparison, endogenous FLS2 expression is shown in *FLS2::FLS2-GFP Ws-0* lines (natural *fls2* mutant; i). Root shape is highlighted with propidium iodide (PI) staining cell wall (PI, red). Scale bar, 100 μm. Developmental regions of the roots are labeled: differentiated zone (DZ); elongation zone (EZ); and meristematic zone (MZ). White arrows represent start of *CASP1::FLS2* signal.

(B) Close-up view of FLS2-GFP expression at selected regions of the complemented lines. FLS2 driven by its endogenous promoter is expressed in all tissues in the DZ (i). Note that, in contrast to previous report, low FLS2 expression is observed in epidermis and cortex (white arrow). In the meristem (MZ), *WER* promoter expresses FLS2 specifically in epidermis (ep) and root cap (rc) (ii) and *SHR* promoter in the stele (st) and endodermis (en) (iv). In the DZ, FLS2 is expressed in all tissues under *UBQ10* promoter (v) but is restricted to endodermis with *CASP1* promoter (iii). FLS2-GFP (BlueGreen) is co-visualized with PI-stained cell wall (red). Separated and overlaid channels (right column) are presented. Scale bar, 25 μm. c, cortex; en, endodermis; ep, epidermis; rc, root cap cells; st, stele. Representative pictures are presented. Nine to twelve seedlings over three to four independent biological replicates were analyzed for each genotype. See also Figure S1.

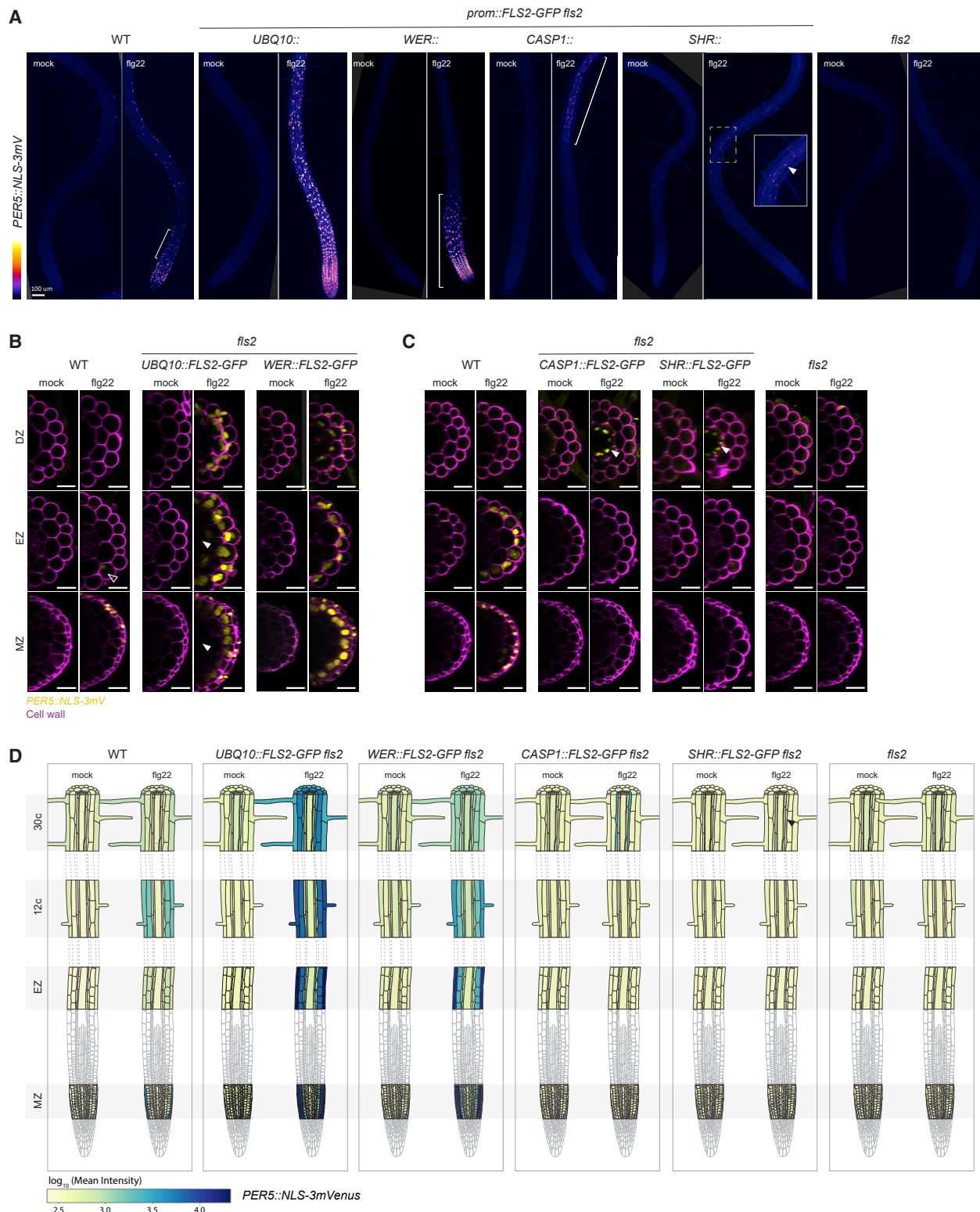
meristem, but induction expands to cortex and pericycle cells in the later root regions (Figures 3C and 3D). Therefore, induction of transcriptional readouts matches largely, but not completely, the FLS2 expression observed in WT plants. Some mismatches—such as the absence of induction in the differentiated stele—despite FLS2 expression there—can be partially explained by the Casparian strip blocking the entry of flg22 into these tissues.<sup>13</sup>

For both markers, changing expression of FLS2 had an obvious impact on the pattern of responses (Figures 2A and 3A). Rather than remaining restricted to the elongation zone, *PER5* and *MYB51* induction largely follows the ectopic FLS2 expression

pattern. The defense markers extend to the whole root in *UBQ10::FLS2*, although they are restricted to the DZ or the MZ in *CASP1::FLS2* and *WER::FLS2*, respectively. As expected, the *fls2* (SAIL691\_C04) mutant does not respond to flg22 in any tissue.

#### **PER5 and MYB51 Appear to Separate Cell-Autonomous and Non-Cell-Autonomous Branches of the MAMP Response**

*PER5* responds only in the differentiated endodermis in the *CASP1::FLS2* recombinant line, which matches the very specific expression pattern of *CASP1* promoter (Figure 2C).



(legend continued on next page)

Sequential captures before and after flg22 treatment allow for visualization of FLS2 receptors and *PER5* marker in the same cells, suggesting a cell-autonomous response (Figure S4A). For *WER::FLS2* line, the *PER5* response also follows detectable *FLS2* expression. We could quantify a strong response in root cap cells and the meristematic epidermis, extending until the early DZ, as well as in cortex cells (Figures 2B–2D), where we could also detect FLS2 protein (Figure S1A). In contrast to *PER5*, we detected *MYB51* response to flg22 not only in cells expressing *FLS2* but also some degree of induction in neighboring cells (Figures 3B–3D). Intensity ratio between flg22 and mock-treated plants were calculated and represented graphically in Figure S4B. Non-cell-autonomous responses seem obvious for *MYB51* in the DZ of *CASP1::FLS2*. Although *FLS2* is specifically expressed in the endodermis (Figures 1Bii and S1B), we could barely detect any *MYB51* responses in this tissue, although the neighboring stele and cortex cells strongly upregulated *MYB51* (Figures 3C, 3D, and S4B). Similarly, flg22 treatment led to strong *MYB51* expression not only in the epidermis and cortex but also in central tissues in *WER::FLS2* (Figures 3C and 3D). Thus, we suggest that *MYB51* induction by MAMPs is controlled by non-cell-autonomous mechanisms, contrasting with the relatively cell-autonomous induction of other markers, such as *PER5* and *FRK1* responses (this work and Zhou et al.<sup>13</sup>).

### FLS2 Expression Is Insufficient to Cause flg22 Responses in the Vascular Meristem

Intriguingly, some tissues were also completely refractory to flg22-triggered responses. Despite a clear presence of FLS2 in the vascular meristem (Figures 1Biv, S1C, and S1D), flg22 treatment did not trigger *PER5* or *MYB51* expression in this tissue in *SHR* and *UBQ10::FLS2* lines (Figures 2 and 3), except for some weak *MYB51* induction in meristematic pericycle cells in *UBQ10::FLS2* (Figures 3D and S4B). Because *SHR::FLS2* is not sufficient to induce *MYB51* in the pericycle cells, despite its expression there, we conclude that flg22 induction of *MYB51* in the pericycle in the *UBQ10::FLS2* line is due to a perception of flg22 in outer cell layers. Thus, central meristematic tissues differ from outer tissue layers in their competence to respond to flg22 in the presence of receptor.

### Regional Ca<sup>2+</sup> Waves Are Initiated from FLS2-Expressing Cells

Because *MYB51* induction by flg22 appeared to have a non-cell-autonomous component, we wondered whether cytosolic calcium increases play a part in non-cell-autonomous flg22 responses. Indeed, cytosolic Ca<sup>2+</sup> increases are among the earliest responses upon MAMP perception, preceding transcriptional changes.<sup>33,34</sup> In roots, Ca<sup>2+</sup> influx after flg22 perception was shown to spread across tissues and was proposed to be part of Ca<sup>2+</sup>/ROS waves, spreading immune signaling over long distances.<sup>23,24,26,27,35</sup> However, because many cells express some degree of *FLS2* in WT plants, it is impossible to dissect to what extent such waves represent a non-cell-autonomous propagation of the Ca<sup>2+</sup> signaling or are due to flg22 diffusion and direct flg22-dependent activation of the receptor in different tissue layers and regions.

Using the intensity-based Ca<sup>2+</sup> reporter *R-GECO1* in our transgenic lines,<sup>26</sup> we observed that, in *WER::FLS2*, calcium signals initiate in the epidermis and spread to inner tissues (Videos S1 and S2; Figures 4A and 4B). Because the receptor has no detectable expression in central tissues, we are taking this as evidence that FLS2 stimulation in epidermis/root cap can cause cytosolic calcium increases in the stele and thus causes a propagating Ca<sup>2+</sup> wave. This propagation of Ca<sup>2+</sup> transients could be observed in all recombinant lines tested, with the intriguing property that the wave direction could be manipulated—i.e., in both *CASP1::FLS2* and *SHR::FLS2* lines, the wave started first in the endodermis then spread to outer and inner tissues (Figures 4C and 4D; Video S2). Moreover, in these two lines, the wave starts in the differentiated rather than in the elongation zone (Video S1). When *FLS2* was expressed in all tissues under the *UBQ10* promoter, all tissues responded almost simultaneously (Figure 4E; Videos S1 and S2). As expected, flg22 does not induce any calcium waves in *fls2* (*SAIL691\_C04*) background (Figure 4F; Video S2). Taken together, although transcriptional readouts are largely cell autonomous, cytosolic calcium transients represent a non-cell-autonomous response to MAMP stimulation. This implies that even cells that are neither exposed to flg22 nor able to perceive this peptide nevertheless rapidly receive a kind of stress signal in the form of a calcium wave.

modified by the different expression patterns of *FLS2*. Brackets indicate responsive regions. For *SHR*, close-up view was generated with increased brightness to highlight stelar signal (white arrow). Scale bar, 100  $\mu$ m.

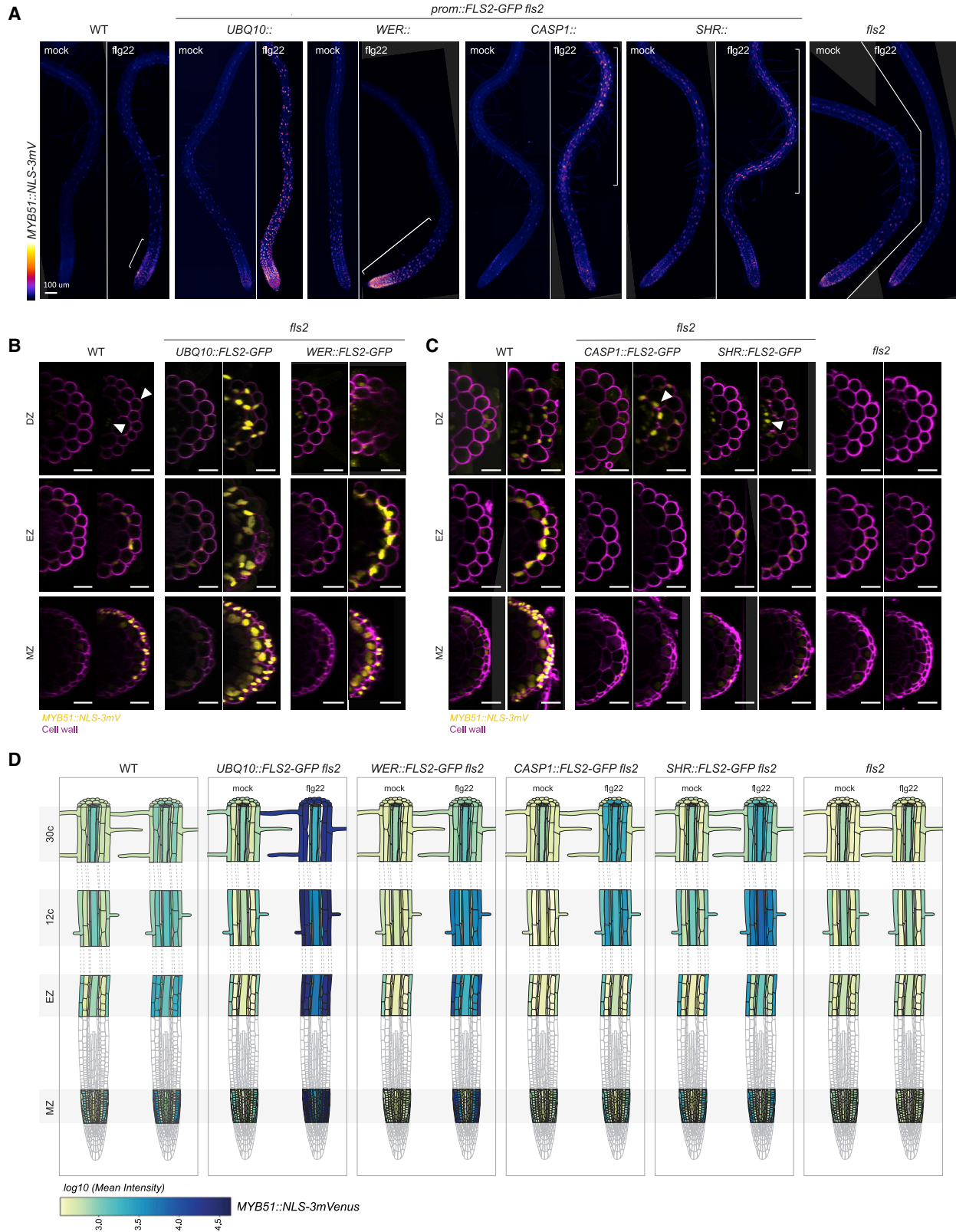
(B) Maximal projection of transverse sections views of *PER5* expression pattern in *UBQ10::* and *WER::FLS2-GFP fls2* compared to WT (*PER5::NLS-3mVenus* in Col-0) shown for MZ, EZ, and DZ (30 cells after start of elongation). Seedlings were treated for 24 h with 1  $\mu$ M flg22. Note the refractory region in the central cylinder in *UBQ10::FLS2-GFP fls2* (white arrows). Nuclear localized mVenus signal (yellow) was co-displayed with PI cell wall marker (purple). Images were taken with similar settings, but corresponding mock and flg22 treatment pictures for each zone separately always have identical parameters. Note that epidermal signal in flg22-treated WT seedlings is faint (EZ, black arrow), due to settings chosen to avoid saturation of signal in the transgenic lines. Compare to (C). WT. Scale bar, 25  $\mu$ m.

(C) Maximal projection of transverse section views of *PER5::NLS-3mVenus* expression pattern in *CASP1::* and *SHR::FLS2-GFP fls2* as well as WT (*PER5::NLS-3mVenus* in Col-0) and *fls2* (*SAIL691\_C04*) control. White arrows point at ectopic response in the endodermis. Images were acquired as in (B), with similar settings between genotypes, but with identical parameter for corresponding mock and flg22 treatment. Pictures were acquired with increased gain compared to (B) due to lower average signal intensity. Scale bar, 25  $\mu$ m.

(A–C) Representative pictures are presented. 10–20 seedlings over 3–5 independent biological replicates were analyzed for each genotype and treatment.

(D) Quantitative map of *PER5::NLS-3mVenus* responses inferred from tissue-specific quantification after 24-h treatment with 1  $\mu$ M flg22. Nuclear signals were quantified in ROI delimited with *UBQ10::NLS-mTurquoise2* for all tissue-specific promoter lines, and WT signal was quantified with *UBQ10::NLS-tdTomato* marker. Mean intensity is therefore comparable between *prom::FLS2-GFP fls2* lines, but not to WT. Four to six seedlings per genotype per treatment were analyzed (n = 51; 16,680 different nuclei analyzed).

See also Figures S2–S4.



(legend on next page)

### Epidermal Meristematic Expression of *FLS2* Leads to flg22 Hypersensitivity and Meristem Collapse

Having demonstrated that we can profoundly alter the pattern of immune responses in the root by ectopic *FLS2* expression, we wanted to study the consequences of such altered spatial patterns for plant growth and defense. Sustained stimulation with MAMPs causes root growth inhibition (RGI) often explained by an antagonism between growth and defense responses.<sup>10</sup> We therefore assessed root length of seedlings transferred to flg22-containing medium (Figures 5A and 5B). As expected, treated WT plants showed only a mild reduction in root length. By contrast, the root length of the constitutive, overexpressing *UBQ10::FLS2* line was strongly reduced with additionally stunted shoot growth. More surprisingly, a strong root length inhibition was also observed in the *WER::FLS2* line, although this line expresses *FLS2* only in young epidermal and root cap cells. *SHR::FLS2* and *CASP1::FLS2*, by contrast, showed root growth similar to WT.

In order to more precisely identify the tissue responsible for root growth inhibition, we generated two additional *prom::FLS2* lines using the *RCH1* (*RECOGNITION OF C. HIGGINSIANUM*) and *PRP3* (*PROLINE-RICH PROTEIN 3*) promoters.<sup>36</sup> *RCH1* is expressed in the whole meristem, although *PRP3* is expressed strongly in differentiating root hair cells (Figure S1E). Although *PER5* induction followed the expression of *FLS2* in both lines (Figures S1G and S1H), only *RCH1::FLS2* presents an increased root growth inhibition, whereas *PRP3::FLS2* responds as WT (Figure S1F). Therefore, we conclude that it is the expression of *FLS2* only in the meristematic epidermal cell layers that causes strongly enhanced root growth inhibition in response to flg22, implying this tissue is extremely sensitive to MAMP responses. Indeed, when comparing the pattern of *PER5* expression between WT and *WER::FLS2* at cellular resolution, it is evident that root cap cells responded strongly to flg22 in both genotypes but that meristematic epidermal cells only show responses in *WER::FLS2* (Figure 5C). This indicates that MAMP responses in meristematic epidermal cells are the cause of the growth inhibition in *WER::FLS2* plants. Importantly, neither the treatment with MAMPs, such as elf18, chitin, or the LPS fragment

3-OH-C10:0, nor the endogenous danger-associated molecular pattern (DAMP) *Atpep1* enhanced *PER5* expression in *WER::FLS2* (Figure 5D). This demonstrates that ectopic *FLS2* expression does not cause a global upregulation of responsiveness to MAMPs or DAMPs but specifically affects flg22-dependent signaling.

Interestingly, treatment of the *WER::FLS2* super-competent line with flg22 induces profound morphological changes in the root not observed in WT. After 2 days of treatment, cells reaching the transition zone start to swell and division patterns become disorganized, giving rise to bulky meristem shapes (Figures 5E, upper panel, and 5G). Virtual cross-sections revealed that cortex cells expand tremendously, dislocating epidermal cells (Figure 5F). Thus, precise spatial regulation of *FLS2* expression levels is necessary to avoid severe root growth inhibition and flg22-induced disorganized cell expansion in the meristem.

### *FLS2* Ectopic Expression Leads to Cell-Autonomous, flg22-Triggered Lignin Deposition

Considering the strong impact of flg22 on meristem morphology in *WER::FLS2*, we decided to assess whether flg22 causes lignin deposition in our lines. Indeed, MAMP responses are known to modify cell wall composition, such as callose deposition or lignification.<sup>8,19,37</sup> Lignin and suberin depositions are long-known damage- and immunity-associated responses<sup>38–43</sup> but have not been widely adopted in recent studies on MTI.<sup>44,45</sup>

We found that flg22 treatment induced strong lignification from transition to differentiated zone in *WER::FLS2* (Figures 5E, lower panel, and S5A). Lignin was deposited between epidermis and cortex cells, mainly at the corners (Figure 5F). In younger regions, lignin was also found between epidermis and root cap cells. Interestingly, all other recombinant lines also showed lignin deposition that coincided with the respective *FLS2* expression patterns, except in the stele (Figure S5). The latter observation corresponded to the absence of flg22-mediated *PER5* induction in these tissues, as can be observed in *SHR::FLS2*, as well as the *GRP::FLS2* line (Figures 2C and S1I) that expresses *FLS2* specifically in the pericycle cells (Figure S1E). Interestingly, no lignin deposition could be observed in flg22-treated WT roots (Figures

#### Figure 3. *MYB51* Marker Is Induced Non-Cell-Autonomously by flg22 Treatment

(A) Overview of *MYB51::NLS-3mVenus* response to 1  $\mu$ M flg22 after 1 day in different *prom::FLS2-GFP fls2* (SAIL691\_C04) lines. *MYB51* zone of responsiveness follows *FLS2* expression pattern. Tile scan images were taken with similar settings. Settings are always identical between mock and corresponding flg22 treatment. Brackets indicate zone of responsiveness. Scale bar, 100  $\mu$ M.

(B) Maximal projection of transverse sections views of *MYB51* expression pattern in *UBQ10::* and *WER::FLS2-GFP fls2* compared to WT shown for MZ, EZ, and DZ (30 cells after start of elongation). Seedlings were treated for 24 h with 1  $\mu$ M flg22. Nuclear localized mVenus signal (yellow) was co-displayed with PI cell wall marker (purple). Images were taken with similar settings, and corresponding mock and flg22 treatment pictures for each zone separately have identical parameters. Pictures were acquired with low gain compare to (C) due to strong average intensity of *UBQ10::* and *WER::FLS2-GFP fls2* responses, explaining the faint signal in WT (white arrowheads). Scale bar, 25  $\mu$ M.

(C) Maximal projection of transverse sections views of *MYB51::NLS-3mVenus* expression in *CASP1::* and *SHR::FLS2* as well as WT and *fls2* (SAIL691\_C04). *MYB51* expression pattern stay conserved (epidermis-cortex-stele), but intensity is increased in neighborhood of cells expressing *FLS2*, such as in cortex in *CASP1::FLS2-GFP fls2* or stele in *SHR::FLS2-GFP fls2* (white arrowheads). Imaged were acquired as in (B), with similar settings between genotypes, and corresponding mock and flg22 treatment pictures have identical parameters. Due to lower average signal intensity, pictures were acquired with increased gain compare to (B). Scale bar, 25  $\mu$ M.

(A–C) 10–20 seedlings over 3–5 independent biological replicates were analyzed for each genotype and treatment.

(D) Quantitative map of *MYB51::NLS-3mVenus* responses inferred from tissue-specific quantification after 24-h treatment with 1  $\mu$ M flg22. Nuclear signals were quantified in ROI delimited with *UBQ10::NLS-mTurquoise2* for all tissue-specific promoter lines, and WT signal was quantified with *UBQ10::NLS-tdTomato* marker. Mean intensity is comparable between *prom::FLS2-GFP fls2* (SAIL691\_C04) lines, but not to WT. Note the constitutive signal present in untreated seedlings. WT represents Col-0 background throughout the whole figure. Three to six seedlings per genotype per treatment were analyzed (n = 59; 15,180 different nuclei analyzed).

See also Figures S2–S4.

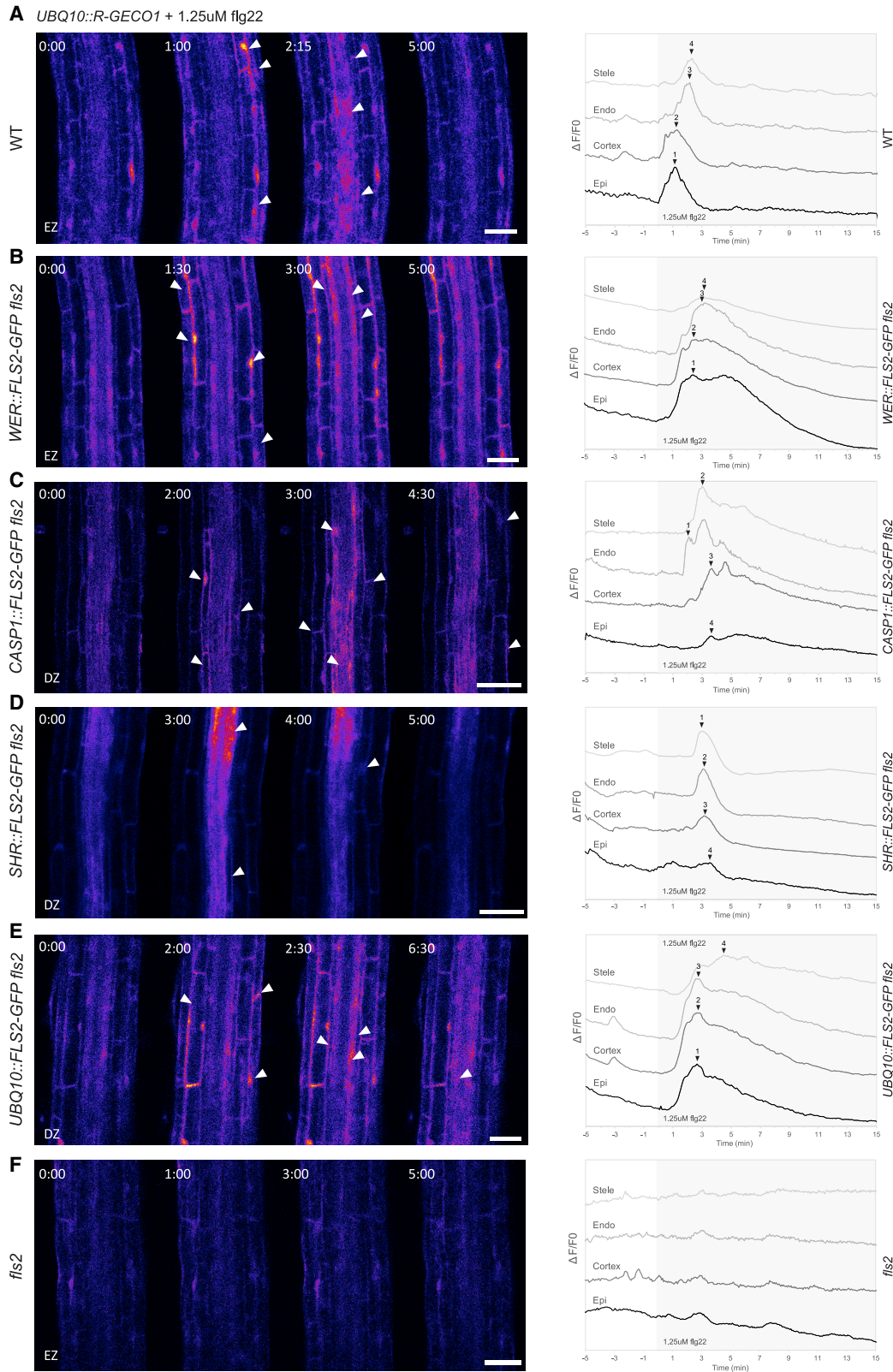


**Figure 4.  $Ca^{2+}$  Waves Are Non-Cell-Autonomous Responses**

$Ca^{2+}$ -dependent signal in (A) WT (Col-0 background) and (B) *WER::FLS2-GFP fls2*, (C) *CASP1::FLS2-GFP fls2*, (D) *SHR::FLS2-GFP fls2*, (E) *UBQ10::FLS2-GFP fls2*, and (F) *fls2* (SAIL691\_C04) lines in response to 1.25  $\mu$ M flg22. Time series of *UBQ10::R-GECO1* fluorescence: pictures are longitudinal middle sections of

(legend continued on next page)

5E, 5F, and S5), fitting with previous reports.<sup>37</sup> It is intriguing to speculate that *PER5*, ROS production, and other flg22-responsive genes, categorized as “oxidative stress” response genes,<sup>46</sup> are actually part of a lignification response that stays below a productive threshold in WT but pivots into a full lignification upon flg22 stimulation of *FLS2* overexpression lines.

### Lignin Deposition Is Not Sufficient to Explain the Strong, flg22-Induced Root Growth Inhibition

The stronger root growth inhibition observed in the super-competent *WER::FLS2* line could be due to the impact of lignin deposition in the transition zone. To test whether cell wall reinforcement by lignin prevents cell division and elongation, we inhibited lignin formation with the monolignol synthesis inhibitor piperonylic acid (PA), expecting to restore root growth. However, even when lignin was no longer detectable, *WER::FLS2* still showed root meristem collapse (Figure 5I) and root growth inhibition (Figure 5H). The rather weak and slow root growth inhibition observed in WT plants is not associated with meristem collapse or lignification, suggesting that this growth inhibition is more indirectly related to immune activation in other tissues and organs.

### Suberin Lamellae Deposition after flg22 Treatment Is an Endodermis-Specific Response

In the root endodermis, ectopic lignin deposition occurs as a compensatory mechanism for impaired Casparian strip formation in a manner similar to lignification in *CASP1::FLS2* lines treated with flg22. In the endodermis, compensatory lignification is often followed by suberin lamellae deposition.<sup>47</sup> We therefore investigated whether flg22 treatment would induce suberin deposition in the endodermis-expressing *FLS2* lines. In WT plants, suberin deposition is usually restricted to the endodermis, starting in the late differentiation zone by patches (“patchy zone”) and then progressing to a fully suberized zone.<sup>48,49</sup> Although no suberin induction by flg22 was found in WT (Figures 6A and 6B), lines expressing *FLS2* in the endodermis, such as *CASP1::*, *SHR::*, and *UBQ10::FLS2*, showed increased endodermal suberization, leading to a complete disappearance of the patchy zone (Figure 6B). *WER::FLS2* roots, by contrast, displayed a normal proportion of patchy to fully suberized zone despite a shorter root length (Figure 6A). Conversely, root growth was not affected in *CASP1::* and *SHR::FLS2* lines, but suberin formed nevertheless much earlier in response to flg22. Therefore, flg22 can induce suberization only when *FLS2* is expressed in the endodermis and suberization can be seen as a cell-type-specific flg22 response.

### Super-competent *WER::FLS2* Plants Can Detect Native Bacterial Flagellin

The strong impact of flg22 on *WER::FLS2* root growth and cell wall modification prompted us to evaluate whether commensal bacteria stimulate similar MAMP responses. Plants that mount

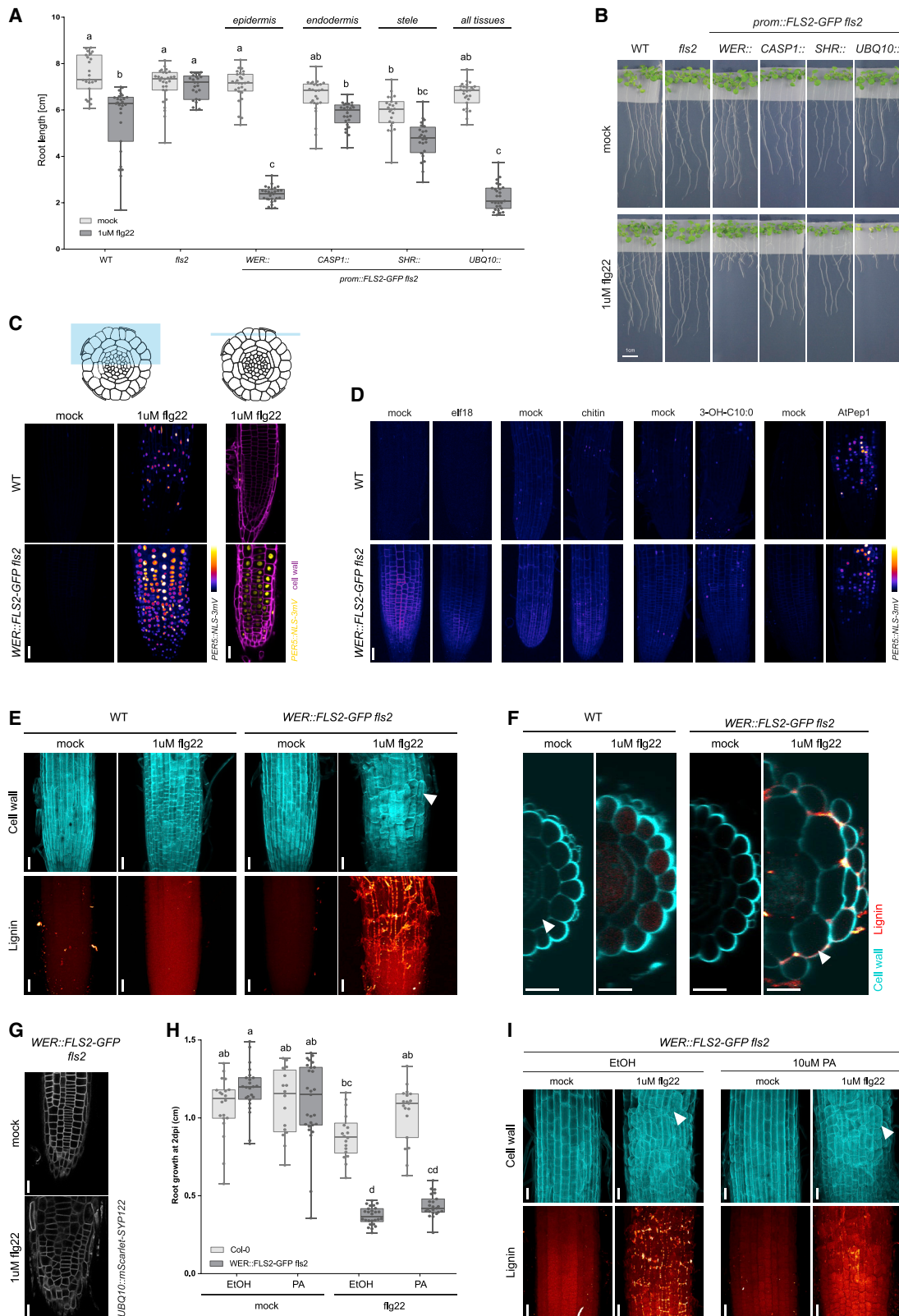
ectopic defenses in sensitive tissues might suffer from the presence of normally harmless bacteria and tip the balance between growth and defense. The model commensal/beneficial *Pseudomonas protegens* CHA0 does not induce MAMP responses in WT plants, except at high concentration or if the root is wounded.<sup>13</sup> However, when CHA0 was inoculated on roots of *WER::FLS2* seedlings in the absence of synthetic flg22 peptide, a strong *PER5* induction was observed (Figure 7A).

To confirm that the induction of *PER5* was caused by native, bacterial flg22, we inoculated seedlings with a CHA0 deletion mutant defective for *fleQ*, which is required for the induction of flagellum development,<sup>50,51</sup> as well as *fliC*, coding for the flagellin protein itself.<sup>52</sup> In contrast to the WT strain,  $\Delta fleQ$  and  $\Delta fliC$  mutants could not trigger any response in *WER::FLS2* and demonstrating that MAMP responses are induced by the direct *FLS2*-mediated detection of bacteria-derived flagellin molecules (Figure 7A). In order to exclude that the absence of *PER5* induction might be due to the impaired motility of the mutants (Figure S6A), we inoculated both plant genotypes with the CHA0 insertion mutant *fliC::pEMG*, which produces non-functional flagellin, including the flg22 sequence, due to the insertion of the pEMG plasmid (Figure S6B). Despite being equally impaired in motility (Figure S6A), we found that *fliC::pEMG* mutant induces *PER5* as efficiently as WT CHA0 strains (Figure 7A), excluding that impaired motility underlies the absence of *PER5* induction in  $\Delta fleQ$  and  $\Delta fliC$  mutants. We also ascertained that all bacterial mutants were in direct contact with root epidermal cells (Figure S6C) and that both mutant and WT bacteria were alive, as shown by colony-forming unit (CFU) counting from colonized roots (Figure S6D). Although  $\Delta fleQ$  mutant colonization was slightly impaired, the  $\Delta fliC$  mutant showed similar CFU counts. Finally, heat-killed CHA0 WT bacteria and *fliC::pEMG* mutants, but not  $\Delta fleQ$  and  $\Delta fliC$  mutants, induce *PER5* (Figure S6E). Together, this clearly indicates that the MAMP responses in the super-competent *WER::FLS2* line are caused exclusively by native flg22 released from the bacteria.

### Root Colonization with *P. protegens* Does Not Cause Enhanced Root Growth Inhibition in *WER::FLS2*

We then assessed the impact of CHA0 bacteria on root growth. Surprisingly, despite its induction of *PER5*, CHA0 did not significantly cause significant root growth inhibition in *WER::FLS2* compared to WT in most replicates (Figure 7B). It has been reported that some commensal bacteria are able to attenuate MAMP-triggered immune responses, either broadly or only the branches of the response that causes root growth inhibition,<sup>53,54</sup> which could explain this observation. Indeed, Ma et al.<sup>55</sup> were unable to observe any growth phenotype of *WER::FLS2* plants grown in non-sterile soil, which they explain by their finding that 41% of root commensals can suppress MAMP-triggered root growth inhibition in mono-associations.<sup>55</sup> Interestingly, they found that only a part of flg22-transcriptional responses were inhibited by a suppressive synthetic bacterial community,

roots at the EZ or DZ. Time 0:00 corresponds to the start of flg22 treatment. White arrows point at tissues showing a strong increase in  $Ca^{2+}$  content. Scale bar, 50  $\mu m$ . Right panel shows normalized R-GECO1 fluorescence intensity ( $\Delta F/F$ ) measured in tissue-specific ROIs. Values present the dynamics of  $Ca^{2+}$  cytosolic concentration in response to flg22 in a single root shown in left panel for each tissue type. Black arrows point at the maximum intensity of the trace. Gray background corresponds to flg22 treatment. Representative pictures are presented. Eight to fifteen seedlings over two to six independent biological replicates were analyzed for each genotype. Quantification was performed on at least three seedlings with similar results. See also Videos S1 and S2.



(legend on next page)

suggesting that suppression of root growth inhibition can be achieved without full suppression of all transcriptional responses.

### **WER::FLS2 Shows Enhanced Root Growth Inhibition to a Restricted Subset of Commensal Bacteria**

In order to obtain a more comprehensive picture of how *WER::FLS2* affects responses to bacteria, we screened a set of 34 bacterial strains from the At-SPHERE culture collection of root-derived commensals<sup>56</sup> (Table S1) for both induction of *PER5* marker and enhanced root growth inhibition in *WER::FLS2* compared to WT lines. We selected isolates to represent different phyla, with a bias toward bacteria predicted by Garrido-Oter et al.<sup>53</sup> to possess a flg22 peptide sequence recognized by FLS2, based on sequence homology with the canonical flg22 sequence (Table S2). We also included some bacteria not predicted to be detected by FLS2. Among the 17 strains predicted to be recognized, only ten triggered an enhanced *PER5* marker induction in *WER::FLS2* (Figure 7C). Moreover, five strains, with flg22 sequences predicted not to be detectable, did induce the *PER5* marker. This underlines the limitations in computationally predicting flg22 activity from sequence alone and the potential of the *WER::FLS2* line to rapidly test experimentally, using living and heat-killed bacteria, whether a native bacterial flg22 can be detected by the plant.

Although half of the bacterial isolates could induce *PER5* marker specifically in the *WER::FLS2* line in our conditions, most of them did not cause enhanced root growth inhibition (Figure 7C; Table S2). However, five of these isolates did show an enhanced effect on *WER::FLS2* root growth compared to WT,

though often with great variation. However, one *Pseudomonas* isolate, R569, caused strongly enhanced *PER5* induction (Figure 7D) and root growth inhibition compared to WT (Figure 7E). For this isolate, the effect was very robust and was repeatedly observed both in Lausanne and Cologne laboratory growth conditions (Figure S6F). We demonstrated that synthesized flg22 from isolate R569 (flg22<sub>R569</sub>) induced *PER5* marker expression and root growth inhibition similarly to the “standard” flg22 from *Pseudomonas aeruginosa* (Figures S6G and S6H). These effects were absent in the *fls2* (SAIL691\_C04) mutant background. In addition, R569, but also the CHA0, *Pseudomonas* strains induce lignin deposition in *WER::FLS2*, but not in WT plants (Figure 7F). We conclude that mis-localized defense activation in the *WER::FLS2* line can lead to strong root growth inhibition in response to a root commensal isolate that is innocuous when growing on WT roots.

### **DISCUSSION**

It is not understood why only a restricted subset of root tissues directly respond to MAMPs in the absence of other stimuli.<sup>13,19,20</sup> The combination of tissue-specific receptor expression and cellular resolution readouts presented here demonstrates the consequences of altering the spatial patterns of MAMP responses in roots and reveals four important features.

First, different MAMP responses are highly tissue specific and varying in cell autonomy. Suberin, for example, is only induced in the endodermis, although lignification can be induced in a wider variety of tissues by FLS2 expression. Although *PER5* induction appears cell autonomous, *MYB51* and calcium signals are also

### **Figure 5. Epidermal Meristematic Expression of FLS2 Leads to flg22 Hypersensitivity and Meristem Collapse**

(A) Flg22 treatment increases root growth inhibition in *WER::FLS2* hypersensitive line. Root length quantification of *prom::FLS2-GFP fls2* lines, *fls2* (SAIL691\_C04) mutant, and WT (Col-0 background) transferred on 1  $\mu$ M flg22 for 6 days post-inoculation (dpi). Boxplot center represents the median ( $n = 23$ –28 roots). Different letters indicate statistically significant difference between means by Kruskal-Wallis test and Dunn’s multiple comparison ( $p < 0.05$ ). Similar results were obtained in two biological replicates.

(B) Representative pictures of quantification in (A), seedlings transferred for 6 days on 1  $\mu$ M flg22. Scale bar, 1 cm.

(C) Flg22 induces strongly *PER5::NLS-3mVenus* in the epidermis of *WER::FLS2-GFP fls2* hypersensitive line compared to WT (Col-0 background). On the right, maximum projection of z stacks taken in root tips of plants treated for 24 h with 1  $\mu$ M flg22 or mock is shown. Schematic represents the depth of the z stack. Pictures were taken with identical settings. Scale bar, 25  $\mu$ m. Representative pictures are presented ( $n = 15$  on four replicates).

(D) *WER::FLS2-GFP fls2* hypersensitivity is specific to flg22. *WER::FLS2-GFP fls2* and WT plants (*PER5::NLS-3mVenus* in Col-0 background) were treated for 24 h with either 1  $\mu$ M elf18, 2  $\mu$ g/mL chitin, 1  $\mu$ M 3-OH-C10:0, or 1  $\mu$ M AtPep1. Maximum projection of z stacks taken in root tips is shown. *PER5* induction is highlighted with mVenus (Fire Lookup Table [LUT]). Parameters were identical for mock and treatment. Scale bar, 25  $\mu$ m. Representative pictures are presented ( $n = 12$  on three replicates).

(E) Treatment of *WER::FLS2-GFP fls2* for 2 days with 1  $\mu$ M flg22 induces meristem swelling and lignin deposition. Upper panel shows median projection of calcofluor-white-stained cell wall in the transition zone of the root tip (cyan). Note bulky cells of the epidermis (white arrowhead). Lower panel presents maximum projection of lignin deposition stained with basic fuchsin (red). Lignin accumulates between cells only in *WER::FLS2-GFP fls2* after flg22 treatment. WT represents Col-0 background. Scale bar, 25  $\mu$ m.

(F) Cross-section of pictures in (E). Cell wall stained with calcofluor white (cyan) is co-visualized with lignin stained with basic fuchsin (red). Flg22 treatment induces massive swelling of cortex cells (white arrowheads) only in *WER::FLS2-GFP fls2*. Lignin is principally deposited between epidermal and cortex cells. Epidermal cells are pushed apart by the swelling cortex and are sometimes missing. Scale bar, 25  $\mu$ m.

(E and F) Representative pictures are presented ( $n = 15$ –20 on five replicates).

(G) Epidermal view of plasma membrane visualized by the construct *UBQ10::mScarlet-SYP122* in *WER::FLS2-GFP fls2*. Cell division is disorganized after 1  $\mu$ M flg22 treatment. Scale bar, 25  $\mu$ m.

(H) Inhibition of monolignol synthesis does not rescue meristem flg22-driven increased root growth inhibition of *WER::FLS2-GFP fls2* compared to WT (Col-0 background). Root growth measured after overnight pre-treatment with 10  $\mu$ M PA inhibitor followed by 36 h 1  $\mu$ M flg22 combined to 10  $\mu$ M PA treatment is shown. Boxplot center represents the median ( $16 \leq n \leq 27$ ). Different letters indicate statistically significant difference ( $p < 0.05$ ) between means by Kruskal-Wallis test and Dunn’s multiple comparison. Similar results were obtained in two biological replicates.

(I) Flg22 induces meristem swelling despite inhibition of monolignol by PA treatment. Pictures were taken from samples quantified in (H). Upper panel shows median projection of calcofluor-white-stained cell wall in the transition zone of root tip (cyan). Lower panel presents maximum projection of lignin deposition stained with basic fuchsin (red). White arrowheads point at examples of bulky cells. Representative pictures are presented. Scale bar, 25  $\mu$ m.

See also Figure S5.

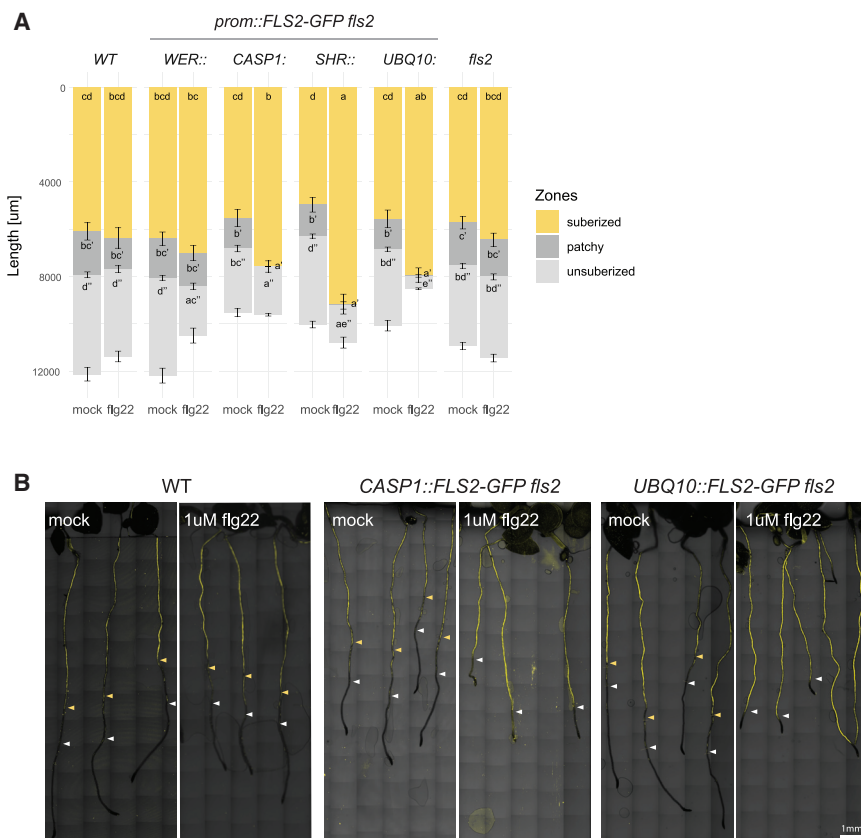


**Figure 6. Suberin Deposition Is Triggered by flg22 when Endodermal Cells Expressed FLS2**

(A) Quantification of suberized zone length in seedlings treated for 1 day with 1  $\mu\text{M}$  flg22 ( $18 \leq n \leq 27$ ). Data of two replicates were pooled. Roots regions were classified as suberized, patchy, and unsuberized zones. Error bars represent standard error (SE). Different letters indicate statistically significant difference among lines for the specified zone ( $p < 0.05$ ). Multiple comparison was performed using ANOVA and Tukey's tests for the suberized zone, whereas Kruskal-Wallis and Dunn's tests were used for patchy and non-suberized zones.

(B) Whole root views of suberin lamellae deposition in *CASP1::* and *UBQ10::FLS2-GFP fls2* lines compared to WT (*Col-0* background) after 1  $\mu\text{M}$  flg22 treatment versus mock. Suberin was stained with Fluorol Yellow. Representative pictures from quantification in (A) are presented. White arrowheads, start of patchy zone; yellow arrowheads, start of fully suberized zones. Scale bar, 1 mm.

induced in cells lacking detectable FLS2 receptor expression. It will be important to describe larger numbers of response genes for a comprehensive view of the cell-type-specific, cell-autonomous, and non-cell-autonomous branches of the flg22 response. Cell-type-specific transcriptomic approaches, for example, can contribute to our understanding of tissue-specific immune pathways.<sup>57</sup> The *prom::FLS2* lines analyzed here can be valuable tools to distinguish cell-autonomous responses from non-cell-autonomous MAMP responses.

Second, we found that the vascular meristem is refractory to flg22 even when expressing FLS2 receptor. The seemingly contradictory finding to Wyrsh et al.<sup>21</sup> can be explained by the whole-organ readouts used in the earlier work, as well as use of *LBD16::FLS2*, thought to be a stele-specific line but that we found to also express in other tissues (Figure S1J). Lack of downstream signaling components or increased activity of negative regulators could both be responsible for the stele's inability to respond to flg22. The vascular meristem might be particularly vulnerable to an activation of defense as it contains early-differentiating phloem, providing nutrition and hormones to the entire growing meristem.

Third, we observed root regions that can be rendered supercompetent by FLS2 expression. We speculate that epidermal meristematic cells are kept non-responsive in WT,<sup>13,19</sup> because the outer root cap cells can mount MAMP responses that are not detrimental to meristem function. This might be linked to the particular fate of root cap cells that rapidly enter apoptosis once they reach the transition zone.<sup>58,59</sup> They do not contribute to the body of the root but excrete mucilage and secondary

metabolites influencing root microbiota.<sup>17,59</sup> However, epidermal cells might need to have a competency for strong responses if root cap damages by pathogens or other stresses induce FLS2 expression. Yet a constitutive expression of FLS2 in the meristematic epidermis leads to drastic changes in the root structure upon exposure to flg22, strongly affecting meristem activity and growth. This inhibition of root growth is faster, much more severe, and possibly of a different nature than the rather weak and slow root growth inhibition observed upon flg22 treatment of WT roots.

Finally, despite lignification upon actual bacterial infection being well documented and shown to restrict bacterial invasion,<sup>8,60,61</sup> treatment with single MAMPs was rarely seen to stimulate lignin deposition, particularly in roots.<sup>37,62–64</sup> Here, we show that strong FLS2 expression enables a single MAMP to induce lignification, probably by overriding endogenous negative feedbacks that prevent this from happening at WT receptor levels. This provides an opportunity to study MAMP-induced lignification in a simplified and reproducible setting. Interestingly, overstimulation of the developmental SCHENGEN pathway also leads to ectopic lignification, as well as defense gene induction, suggesting unexpected commonalities between developmental and immune receptor pathways.<sup>65–68</sup> Nevertheless, lignification only partly explains the severe root growth inhibition we observe. Other factors produced in response to flg22 might also interfere with meristem function, such as basic coumarins,<sup>69</sup> which inhibit cellulose biosynthesis, resulting in meristem swelling similar to the one observed on *WER::FLS2*.<sup>70</sup>

Importantly, our work also reveals that overexpression of a single PRR in a competent but otherwise non-responsive cell type bypasses the weak or absent immune responses to commensal bacteria.<sup>13,19,53,71</sup> Though bacteria can inhibit MTI,<sup>12,72</sup> MAMPs produced by rhizosphere bacteria might often be too low in

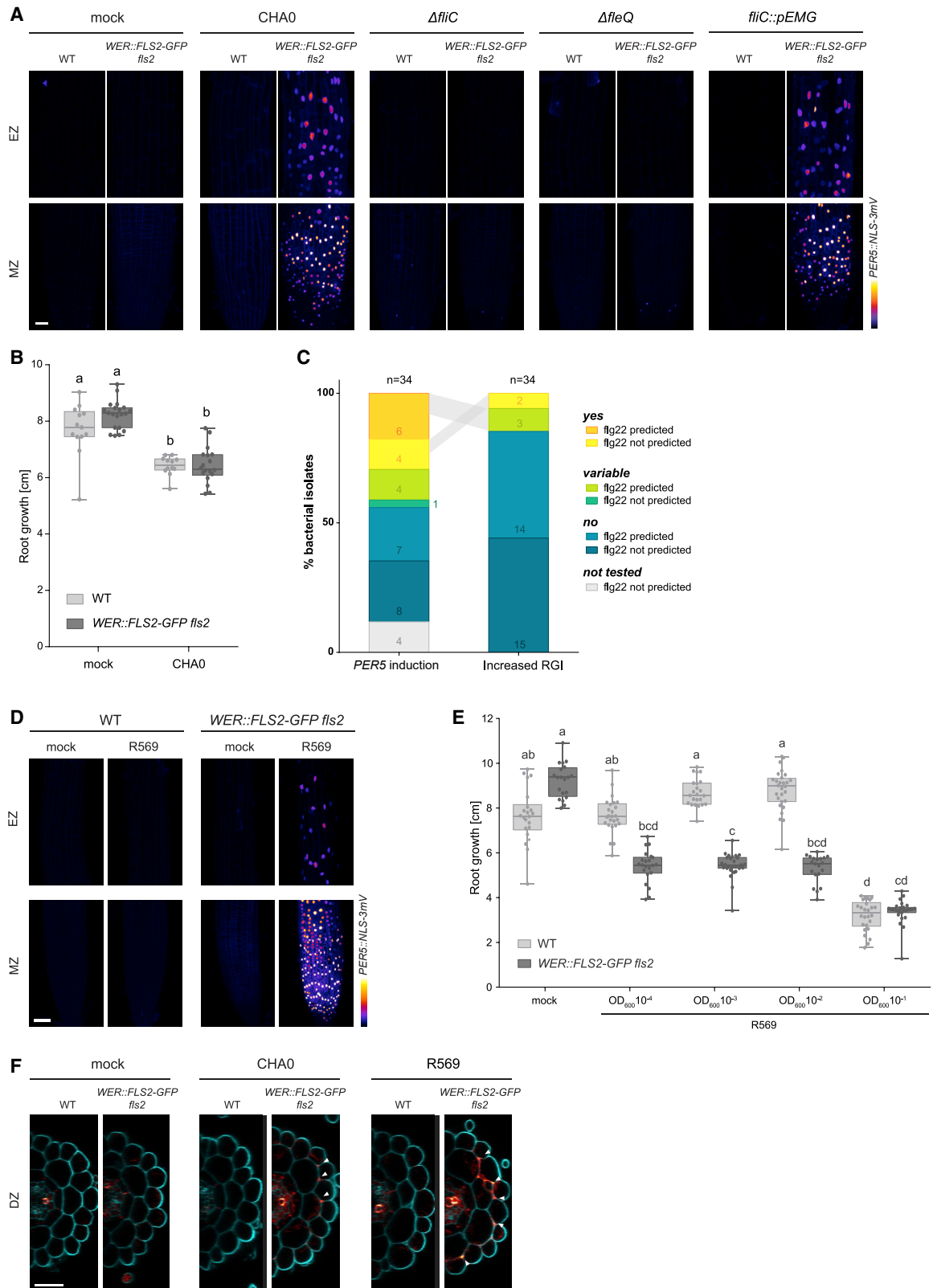


**Figure 7. WER::FLS2 Line Detects Endogenous Bacterial flg22**

(A) CHA0 bacteria trigger a strong induction of *PER5::NLS-3mVenus* marker (Fire LUT) on *WER::FLS2-GFP fls2* compared to WT (Col-0 background). Mutants  $\Delta fliC$  and  $\Delta fleQ$  defective for flagellum lose their ability to induce detectable MAMP responses. The *fliC::pEMG* mutant presenting non-functional flagellin still

(legend continued on next page)

concentration to activate MAMP responses in the first place. Therefore, roots can appear largely unresponsive to bacterial presence without additional stresses.<sup>13</sup> The obvious root growth phenotype triggered by MAMPs in *WER::FLS2* lines proves to be a powerful tool to investigate the effect of commensals on root immune responses. Our super-competent lines have allowed for the first time to demonstrate stimulation of FLS2 by a native flagellin peptide from a commensal bacterium. Generally, the cocktail of elicitors that bacteria is thought to release prevents assignment of a MAMP response to an individual MAMP.<sup>73</sup> The *WER::FLS2* line now generates a cell type that responds only to a single MAMP and can test predictions about flg22 peptide detectability, release, and processing. Extending our approach, the ectopic overexpression of potential PRR receptors in the epidermal meristem cells could be used to functionally pair novel receptors and ligands.

It has become evident that immune responses cannot be understood without taking into consideration the specificities of different cell types and developmental stages. Our data establish the necessity for the plant to spatially restrict its immune responses. This spatial allocation of defense capacities might in turn influence the microbial colonization pattern of the rhizosphere. The new tools presented will pave the way for a better understanding of bacterial community structures in roots.

## STAR★METHODS

Detailed methods are provided in the online version of this paper and include the following:

- **KEY RESOURCES TABLE**
- **RESOURCE AVAILABILITY**
  - Lead Contact
  - Materials Availability
  - Data and Code Availability
- **EXPERIMENTAL MODEL AND SUBJECT DETAILS**
  - Plant material

- Plant growth conditions
- Bacterial strains and growth conditions
- **METHOD DETAILS**
  - Plant plasmid construction
  - Elicitors and inhibitors treatments
  - Microscopy settings and image processing
  - Fixation and staining
  - Ca<sup>2+</sup> imaging on roots
  - Suberin staining
  - Bacterial root inoculation assays
  - CFU counting
  - Swimming assay
- **QUANTIFICATION AND STATISTICAL ANALYSIS**

- Cell-specific quantification
- Calcium signaling quantification
- Statistical analysis

## SUPPLEMENTAL INFORMATION

Supplemental Information can be found online at <https://doi.org/10.1016/j.cub.2020.12.048>.

## ACKNOWLEDGMENTS

We thank the Central Imaging Facility (CIF) of the University of Lausanne for expert technical support. We particularly thank Thomas Boller (Basel), Jean-Pierre Métraux (Fribourg), Silke Lehman (Fribourg), and Ines Wyrsh (Basel) for initiating this project with us. We thank Youssef Belkhadir (Vienna), Thorsten Nürnberger (Tübingen), Corné Pieterse (Utrecht), Cyril Zipfel (Zürich), and Peter Kupferschmied (Bern) as well as all members from the Geldner lab for sharing material and/or helpful discussions and input. Finally, we are grateful to Artan Graf and Yasmine Genolet for their patience and assiduity for the manual curation of cell-type-specific quantification. This work was supported by funds to N.G. from an ERC Consolidator Grant (GA-N: 616228-ENDOFUN) and two consecutive Swiss National Science Foundation (SNSF) grants (CRSII3\_136278 and 31003A\_156261). F.Z. was supported by a European Molecular Biology Organization (EMBO) Long-Term Fellowship (ALTF 1139-2014) and A.E. by an EMBO Short-Term Fellowship (STF8066).

induces *PER5* transcriptional readout. Maximum projection of z stacks imaging MZs and EZs treated with drop inoculation of bacterial solution of a concentration of optical density 600 ( $OD_{600}$ ) = 0.01 or mock, respectively, is shown. Representative images were acquired at 1 dpi ( $n = 15$  on five replicates). Acquisition was done with identical settings. Scale bar, 25  $\mu$ m.

(B) CHA0 does not induce consistently increased root growth inhibition in *WER::FLS2-GFP fls2* compared to WT (Col-0 background). Root growth was quantified at 6 dpi on plate inoculated with bacteria at  $OD_{600} = 10^{-3}$ . Different letters indicate statistically significant difference ( $p < 0.05$ ). Multiple comparison was performed using ANOVA and Tukey's test ( $n = 12-20$ ). Similar results were obtained in half our replicates (5/10). In the other half, CHA0 induced a small, often non-significant RGI.

(C) Proportion of natural isolates from At-SPHERE culture collection triggering stronger *PER5::NLS-3mVenus* induction and increased RGI on *WER::FLS2-GFP fls2* compared to WT seedlings (*PER5::NLS-3mVenus* in Col-0 background; yes) or not (no). Bacteria classified in "variable" presented contradictory results between replicates. Bacteria flg22 sequence was predicted to be recognized by FLS2 (flg22 predicted) or not (flg22 not predicted). Numbers of bacterial isolates in each category are indicated in color. Gray surfaces indicate identical bacteria strains.

(D) *Pseudomonas* isolate R569 from At-SPHERE culture collection triggers strong *PER5::NLS-3mVenus* (Fire LUT) induction on *WER::FLS2-GFP fls2*, but not in WT (Col-0 background). Seedlings were imaged after 1-day treatment with  $OD_{600} = 0.01$ . Maximum projection of z stacks at MZ and EZ is shown. Scale bar, 50  $\mu$ m. Representative pictures are presented. Nine to twelve seedlings over three independent biological replicates were analyzed for each genotype and treatment.

(E) Isolate R569 induces a robust increased root growth inhibition on *WER::FLS2-GFP fls2* compared to WT plants (Col-0 background). High concentration of bacteria ( $OD_{600} = 0.1$ ) is deleterious to both genotypes. Root growth was quantified at 6 dpi on plates inoculated with bacteria at  $OD_{600} = 10^{-1}$  to  $10^{-4}$ . Different letters indicate statistically significant difference ( $p < 0.05$ ). Multiple comparison was performed using Kruskal-Wallis and Dunn's test ( $n = 20-27$  by genotype by treatment). Similar results were obtained in at least three replicates.

(F) Treatment of *WER::FLS2-GFP fls2* for 3 days with 2  $\mu$ L of CHA0 or R569 bacterial solution ( $OD_{600} = 0.01$ ) induces lignin deposition (RedHot LUT) between the epidermis and cortex of the differentiated zone. Cell wall is highlighted with calcofluor white (cyan). Representative images are presented ( $n = 10$  on two replicates). White arrowhead, lignin deposition. Scale bar, 25  $\mu$ m.

See also [Figure S6](#) and [Tables S1](#) and [S2](#).

### AUTHOR CONTRIBUTIONS

A.E. and N.G. conceived, designed, and coordinated the project. A.E., F.Z., J.V., C.M.H., and V.D.T. performed all experimental work. A.E. and N.G. wrote the manuscript. A.E., F.Z., J.V., K.-W.M., P.S.-L., C.K., and N.G. revised the manuscript and were involved in the discussion of the work.

### DECLARATION OF INTERESTS

The authors declare no competing interests.

Received: August 11, 2020

Revised: October 27, 2020

Accepted: December 24, 2020

Published: January 27, 2021

### REFERENCES

1. Lebeis, S.L., Paredes, S.H., Lundberg, D.S., Breakfield, N., Gehring, J., McDonald, M., Malfatti, S., Glavina del Rio, T., Jones, C.D., Tringe, S.G., and Dangl, J.L. (2015). Plant microbiome. Salicylic acid modulates colonization of the root microbiome by specific bacterial taxa. *Science* **349**, 860–864.
2. Rooks, M.G., and Garrett, W.S. (2016). Gut microbiota, metabolites and host immunity. *Nat. Rev. Immunol.* **16**, 341–352.
3. Zipfel, C. (2008). Pattern-recognition receptors in plant innate immunity. *Curr. Opin. Immunol.* **20**, 10–16.
4. Felix, G., Duran, J.D., Volko, S., and Boller, T. (1999). Plants have a sensitive perception system for the most conserved domain of bacterial flagellin. *Plant J.* **18**, 265–276.
5. Gómez-Gómez, L., and Boller, T. (2000). FLS2: an LRR receptor-like kinase involved in the perception of the bacterial elicitor flagellin in *Arabidopsis*. *Mol. Cell* **5**, 1003–1011.
6. Gómez-Gómez, L., Felix, G., and Boller, T. (1999). A single locus determines sensitivity to bacterial flagellin in *Arabidopsis thaliana*. *Plant J.* **18**, 277–284.
7. Zipfel, C., Robatzek, S., Navarro, L., Oakeley, E.J., Jones, J.D.G., Felix, G., and Boller, T. (2004). Bacterial disease resistance in *Arabidopsis* through flagellin perception. *Nature* **428**, 764–767.
8. Lee, M.-H., Jeon, H.S., Kim, S.H., Chung, J.H., Roppolo, D., Lee, H.-J., Cho, H.J., Tobimatsu, Y., Ralph, J., and Park, O.K. (2019). Lignin-based barrier restricts pathogens to the infection site and confers resistance in plants. *EMBO J.* **38**, e101948.
9. Li, B., Meng, X., Shan, L., and He, P. (2016). Transcriptional regulation of pattern-triggered immunity in Plants. *Cell Host Microbe* **19**, 641–650.
10. Chinchilla, D., Zipfel, C., Robatzek, S., Kemmerling, B., Nürnberger, T., Jones, J.D.G., Felix, G., and Boller, T. (2007). A flagellin-induced complex of the receptor FLS2 and BAK1 initiates plant defence. *Nature* **448**, 497–500.
11. Berendsen, R.L., Pieterse, C.M.J., and Bakker, P.A.H.M. (2012). The rhizosphere microbiome and plant health. *Trends Plant Sci.* **17**, 478–486.
12. Yu, K., Pieterse, C.M.J., Bakker, P.A.H.M., and Berendsen, R.L. (2019). Beneficial microbes going underground of root immunity. *Plant Cell Environ.* **42**, 2860–2870.
13. Zhou, F., Emonet, A., Dénervaud Tendon, V., Marhavy, P., Wu, D., Lahaye, T., and Geldner, N. (2020). Co-occurrence of damage and microbial patterns controls localized immune responses in roots. *Cell* **180**, 440–453.e18.
14. Beck, M., Wyrsh, I., Strutt, J., Wimalasekera, R., Webb, A., Boller, T., and Robatzek, S. (2014). Expression patterns of *flagellin sensing 2* map to bacterial entry sites in plant shoots and roots. *J. Exp. Bot.* **65**, 6487–6498.
15. Faulkner, C., and Robatzek, S. (2012). Plants and pathogens: putting infection strategies and defence mechanisms on the map. *Curr. Opin. Plant Biol.* **15**, 699–707.
16. Munch, D., Gupta, V., Bachmann, A., Busch, W., Kelly, S., Mun, T., and Andersen, S.U. (2018). The *Brassicaceae* family displays divergent, shoot-skewed NLR resistance gene expression. *Plant Physiol.* **176**, 1598–1609.
17. Bulgarelli, D., Schlaeppi, K., Spaepen, S., Ver Loren van Themaat, E., and Schulze-Lefert, P. (2013). Structure and functions of the bacterial microbiota of plants. *Annu. Rev. Plant Biol.* **64**, 807–838.
18. De Coninck, B., Timmermans, P., Vos, C., Cammue, B.P.A., and Kazan, K. (2015). What lies beneath: belowground defense strategies in plants. *Trends Plant Sci.* **20**, 91–101.
19. Millet, Y.A., Danna, C.H., Clay, N.K., Songnuan, W., Simon, M.D., Werck-Reichhart, D., and Ausubel, F.M. (2010). Innate immune responses activated in *Arabidopsis* roots by microbe-associated molecular patterns. *Plant Cell* **22**, 973–990.
20. Poncini, L., Wyrsh, I., Dénervaud Tendon, V., Vorley, T., Boller, T., Geldner, N., Métraux, J.-P., and Lehmann, S. (2017). In roots of *Arabidopsis thaliana*, the damage-associated molecular pattern AtPep1 is a stronger elicitor of immune signalling than flg22 or the chitin heptamer. *PLoS ONE* **12**, e0185808.
21. Wyrsh, I., Domínguez-Ferreras, A., Geldner, N., and Boller, T. (2015). Tissue-specific FLAGELLIN-SENSING 2 (FLS2) expression in roots restores immune responses in *Arabidopsis fls2* mutants. *New Phytol.* **206**, 774–784.
22. Dubiella, U., Seybold, H., Durian, G., Komander, E., Lassig, R., Witte, C.-P., Schulze, W.X., and Romeis, T. (2013). Calcium-dependent protein kinase/NADPH oxidase activation circuit is required for rapid defense signal propagation. *Proc. Natl. Acad. Sci. USA* **110**, 8744–8749.
23. Gilroy, S., Suzuki, N., Miller, G., Choi, W.-G., Toyota, M., Devireddy, A.R., and Mittler, R. (2014). A tidal wave of signals: calcium and ROS at the forefront of rapid systemic signaling. *Trends Plant Sci.* **19**, 623–630.
24. Gilroy, S., Bialasek, M., Suzuki, N., Görecka, M., Devireddy, A.R., Karpiński, S., and Mittler, R. (2016). ROS, calcium, and electric signals: key mediators of rapid systemic signaling in plants. *Plant Physiol.* **171**, 1606–1615.
25. Marhavy, P., Kurenda, A., Siddique, S., Dénervaud Tendon, V., Zhou, F., Holbein, J., Hasan, M.S., Grundler, F.M., Farmer, E.E., and Geldner, N. (2019). Single-cell damage elicits regional, nematode-restricting ethylene responses in roots. *EMBO J.* **38**, e100972.
26. Keinath, N.F., Waadt, R., Brugman, R., Schroeder, J.I., Grossmann, G., Schumacher, K., and Krebs, M. (2015). Live cell imaging with R-GECO1 sheds light on flg22- and chitin-induced transient  $[Ca^{2+}]_{Cyt}$  patterns in *Arabidopsis*. *Mol. Plant* **8**, 1188–1200.
27. Stanley, C.E., Shrivastava, J., Brugman, R., Heinzemann, E., van Swaay, D., and Grossmann, G. (2018). Dual-flow-RootChip reveals local adaptations of roots towards environmental asymmetry at the physiological and genetic levels. *New Phytol.* **217**, 1357–1369.
28. Vermeer, J.E.M., von Wangenheim, D., Barberon, M., Lee, Y., Stelzer, E.H.K., Maizel, A., and Geldner, N. (2014). A spatial accommodation by neighboring cells is required for organ initiation in *Arabidopsis*. *Science* **343**, 178–183.
29. Thor, K., and Peiter, E. (2014). Cytosolic calcium signals elicited by the pathogen-associated molecular pattern flg22 in stomatal guard cells are of an oscillatory nature. *New Phytol.* **204**, 873–881.
30. Lee, M.M., and Schiefelbein, J. (1999). WEREWOLF, a MYB-related protein in *Arabidopsis*, is a position-dependent regulator of epidermal cell patterning. *Cell* **99**, 473–483.
31. Benfey, P.N., Linstead, P.J., Roberts, K., Schiefelbein, J.W., Hauser, M.T., and Aeschbacher, R.A. (1993). Root development in *Arabidopsis*: four mutants with dramatically altered root morphogenesis. *Development* **119**, 57–70.
32. Helariutta, Y., Fukaki, H., Wysocka-Diller, J., Nakajima, K., Jung, J., Sena, G., Hauser, M.-T., and Benfey, P.N. (2000). The *SHORT-ROOT* gene controls radial patterning of the *Arabidopsis* root through radial signaling. *Cell* **101**, 555–567.
33. Jeworutzki, E., Roelfsema, M.R.G., Anshütz, U., Krol, E., Elzenga, J.T.M., Felix, G., Boller, T., Hedrich, R., and Becker, D. (2010). Early signaling

- through the *Arabidopsis* pattern recognition receptors FLS2 and EFR involves Ca-associated opening of plasma membrane anion channels. *Plant J.* **62**, 367–378.
34. Seybold, H., Trempel, F., Ranf, S., Scheel, D., Romeis, T., and Lee, J. (2014). Ca<sup>2+</sup> signalling in plant immune response: from pattern recognition receptors to Ca<sup>2+</sup> decoding mechanisms. *New Phytol.* **204**, 782–790.
35. Choi, W.-G., Hilleary, R., Swanson, S.J., Kim, S.-H., and Gilroy, S. (2016). Rapid, long-distance electrical and calcium signaling in plants. *Annu. Rev. Plant Biol.* **67**, 287–307.
36. Marqués-Bueno, M.D.M., Morao, A.K., Cayrel, A., Platre, M.P., Barberon, M., Caillieux, E., Colot, V., Jaillais, Y., Roudier, F., and Vert, G. (2016). A versatile multisite gateway-compatible promoter and transgenic line collection for cell type-specific functional genomics in *Arabidopsis*. *Plant J.* **85**, 320–333.
37. Chezem, W.R., Memon, A., Li, F.-S., Weng, J.-K., and Clay, N.K. (2017). SG2-type R2R3-MYB transcription factor MYB15 controls defense-induced lignification and basal immunity in *Arabidopsis*. *Plant Cell* **29**, 1907–1926.
38. Bernards, M.A. (2002). Demystifying suberin. *Can. J. Bot.* **80**, 227–240.
39. Hijwegen, T. (1963). Lignification, a possible mechanism of active resistance against pathogens. *Neth. J. Plant Pathol.* **69**, 314–317.
40. Kamula, S.A., Peterson, C.A., and Mayfield, C.I. (1994). Impact of the exodermis on infection of roots by *Fusarium culmorum*. *Plant Soil* **167**, 121–126.
41. Messner, B., and Boll, M. (1993). Elicitor-mediated induction of enzymes of lignin biosynthesis and formation of lignin-like material in a cell suspension culture of spruce (*Picea abies*). *Plant Cell Tissue Organ Cult.* **34**, 261–269.
42. Ranathunge, K., Thomas, R.H., Fang, X., Peterson, C.A., Gijzen, M., and Bernards, M.A. (2008). Soybean root suberin and partial resistance to root rot caused by *Phytophthora sojae*. *Phytopathology* **98**, 1179–1189.
43. Thomas, R., Fang, X., Ranathunge, K., Anderson, T.R., Peterson, C.A., and Bernards, M.A. (2007). Soybean root suberin: anatomical distribution, chemical composition, and relationship to partial resistance to *Phytophthora sojae*. *Plant Physiol.* **144**, 299–311.
44. Lange, B.M., Lapierre, C., and Sandermann, H., Jr. (1995). Elicitor-induced spruce stress lignin (structural similarity to early developmental lignins). *Plant Physiol.* **108**, 1277–1287.
45. Mandal, S., and Mitra, A. (2007). Reinforcement of cell wall in roots of *Lycopersicon esculentum* through induction of phenolic compounds and lignin by elicitors. *Physiol. Mol. Plant Pathol.* **71**, 201–209.
46. Tognolli, M., Penel, C., Greppin, H., and Simon, P. (2002). Analysis and expression of the class III peroxidase large gene family in *Arabidopsis thaliana*. *Gene* **288**, 129–138.
47. Doblaz, V.G., Smakowska-Luzan, E., Fujita, S., Alassimone, J., Barberon, M., Madalinski, M., Belkhadir, Y., and Geldner, N. (2017). Root diffusion barrier control by a vasculature-derived peptide binding to the SGN3 receptor. *Science* **355**, 280–284.
48. Andersen, T.G., Barberon, M., and Geldner, N. (2015). Suberization - the second life of an endodermal cell. *Curr. Opin. Plant Biol.* **28**, 9–15.
49. Andersen, T.G., Naseer, S., Ursache, R., Wybouw, B., Smet, W., De Rybel, B., Vermeer, J.E.M., and Geldner, N. (2018). Diffusible repression of cytokinin signalling produces endodermal symmetry and passage cells. *Nature* **555**, 529–533.
50. Arora, S.K., Ritchings, B.W., Almira, E.C., Lory, S., and Ramphal, R. (1997). A transcriptional activator, FleQ, regulates mucin adhesion and flagellar gene expression in *Pseudomonas aeruginosa* in a cascade manner. *J. Bacteriol.* **179**, 5574–5581.
51. Kupferschmid, P. (2015). Molecular basis and regulation of insect pathogenicity in plant-beneficial pseudomonads. PhD thesis (UNIL/CHUV).
52. Yamaguchi, S., Fujita, H., Sugata, K., Taira, T., and Iino, T. (1984). Genetic analysis of *H2*, the structural gene for phase-2 flagellin in *Salmonella*. *J. Gen. Microbiol.* **130**, 255–265.
53. Garrido-Oter, R., Nakano, R.T., Dombrowski, N., Ma, K.-W., McHardy, A.C., and Schulze-Lefert, P.; AgBiome Team (2018). Modular traits of the Rhizobiales root microbiota and their evolutionary relationship with symbiotic Rhizobia. *Cell Host Microbe* **24**, 155–167.e5.
54. Pel, M.J.C., and Pieterse, C.M.J. (2013). Microbial recognition and evasion of host immunity. *J. Exp. Bot.* **64**, 1237–1248.
55. Ma, K.-W., Niu, Y., Jia, Y., Ordon, J., Copeland, C., Emonet, A., et al. (2020). Coordination of microbe-host homeostasis via a crosstalk with plant innate immunity. *Research Square*. <https://doi.org/10.21203/rs.3.rs-69445/v1>.
56. Bai, Y., Müller, D.B., Srinivas, G., Garrido-Oter, R., Potthoff, E., Rott, M., Dombrowski, N., Münch, P.C., Spaepen, S., Remus-Emsermann, M., et al. (2015). Functional overlap of the *Arabidopsis* leaf and root microbiota. *Nature* **528**, 364–369.
57. Rich-Griffin, C., Eichmann, R., Reitz, M.U., Hermann, S., Woolley-Allen, K., Brown, P.E., Wiwatdirekkul, K., Esteban, E., Pasha, A., Kogel, K.-H., et al. (2020). Regulation of cell type-specific immunity networks in *Arabidopsis* roots. *Plant Cell* **32**, 2742–2762.
58. Fendrych, M., Van Hautegeem, T., Van Durme, M., Olvera-Carrillo, Y., Huysmans, M., Karimi, M., Lippens, S., Guérin, C.J., Krebs, M., Schumacher, K., and Nowack, M.K. (2014). Programmed cell death controlled by ANAC033/SOMBRERO determines root cap organ size in *Arabidopsis*. *Curr. Biol.* **24**, 931–940.
59. Kumpf, R.P., and Nowack, M.K. (2015). The root cap: a short story of life and death. *J. Exp. Bot.* **66**, 5651–5662.
60. Nicholson, R.L., and Hammerschmidt, R. (1992). Phenolic compounds and their role in disease resistance. *Annu. Rev. Phytopathol.* **30**, 369–389.
61. Vance, C.P., Kirk, T.K., and Sherwood, R.T. (1980). Lignification as a mechanism of disease resistance. *Annu. Rev. Phytopathol.* **18**, 259–288.
62. Adams-Phillips, L., Briggs, A.G., and Bent, A.F. (2010). Disruption of poly(ADP-ribosylation) mechanisms alters responses of *Arabidopsis* to biotic stress. *Plant Physiol.* **152**, 267–280.
63. Robertsen, B. (1986). Elicitors of the production of lignin-like compounds in cucumber hypocotyls. *Physiol. Mol. Plant Pathol.* **28**, 137–148.
64. Smit, F., and Dubery, I.A. (1997). Cell wall reinforcement in cotton hypocotyls in response to a *Verticillium dahliae* elicitor. *Phytochemistry* **44**, 811–815.
65. Alassimone, J., Fujita, S., Doblaz, V.G., van Dop, M., Barberon, M., Kalmbach, L., Vermeer, J.E.M., Rojas-Murcia, N., Santuari, L., Hardtke, C.S., and Geldner, N. (2016). Polarly localized kinase SGN1 is required for Casparian strip integrity and positioning. *Nat. Plants* **2**, 16113.
66. Doblaz, V.G., Geldner, N., and Barberon, M. (2017). The endodermis, a tightly controlled barrier for nutrients. *Curr. Opin. Plant Biol.* **39**, 136–143.
67. Fujita, S., De Bellis, D., Edel, K.H., Köster, P., Andersen, T.G., Schmid-Siegert, E., Dénervaud Tendon, V., Pfister, A., Marhavý, P., Ursache, R., et al. (2020). SCHENGEN receptor module drives localized ROS production and lignification in plant roots. *EMBO J.* **39**, e103894.
68. Pfister, A., Barberon, M., Alassimone, J., Kalmbach, L., Lee, Y., Vermeer, J.E., Yamazaki, M., Li, G., Maurel, C., Takano, J., et al. (2014). A receptor-like kinase mutant with absent endodermal diffusion barrier displays selective nutrient homeostasis defects. *eLife* **3**, e03115.
69. Stringlis, I.A., de Jonge, R., and Pieterse, C.M.J. (2019). The age of coumarins in plant-microbe interactions. *Plant Cell Physiol.* **60**, 1405–1419.
70. Hara, M., Umetsu, N., Miyamoto, C., and Tamari, K. (1973). Inhibition of the biosynthesis of plant cell wall materials, especially cellulose biosynthesis, by coumarin. *Plant Cell Physiol.* **14**, 11–28.
71. Yu, K., Liu, Y., Tichelaar, R., Savant, N., Lagendijk, E., van Kuijk, S.J.L., Stringlis, I.A., van Dijken, A.J.H., Pieterse, C.M.J., Bakker, P.A.H.M., et al. (2019). Rhizosphere-associated *Pseudomonas* suppress local root immune responses by gluconic acid-mediated lowering of environmental pH. *Curr. Biol.* **29**, 3913–3920.e4.
72. Couto, D., and Zipfel, C. (2016). Regulation of pattern recognition receptor signalling in plants. *Nat. Rev. Immunol.* **16**, 537–552.

73. Tang, D., Wang, G., and Zhou, J.-M. (2017). Receptor kinases in plant-pathogen interactions: more than pattern recognition. *Plant Cell* **29**, 618–637.
74. Robatzek, S., Chinchilla, D., and Boller, T. (2006). Ligand-induced endocytosis of the pattern recognition receptor FLS2 in *Arabidopsis*. *Genes Dev.* **20**, 537–542.
75. Clough, S.J., and Bent, A.F. (1998). Floral dip: a simplified method for *Agrobacterium*-mediated transformation of *Arabidopsis thaliana*. *Plant J.* **16**, 735–743.
76. Stutz, E.W., Défago, G., and Kern, H. (1986). Naturally occurring fluorescent pseudomonads involved in suppression of black root rot of tobacco. *Phytopathology* **76**, 181–185.
77. Martínez-García, E., and de Lorenzo, V. (2011). Engineering multiple genomic deletions in Gram-negative bacteria: analysis of the multi-resistant antibiotic profile of *Pseudomonas putida* KT2440. *Environ. Microbiol.* **13**, 2702–2716.
78. Kupferschmied, P., Péchy-Tarr, M., Imperiali, N., Maurhofer, M., and Keel, C. (2014). Domain shuffling in a sensor protein contributed to the evolution of insect pathogenicity in plant-beneficial *Pseudomonas protegens*. *PLoS Pathog.* **10**, e1003964.
79. Siligato, R., Wang, X., Yadav, S.R., Lehesranta, S., Ma, G., Ursache, R., Sevillem, I., Zhang, J., Gorte, M., Prasad, K., et al. (2016). MultiSite gateway-compatible cell type-specific gene-inducible system for plants. *Plant Physiol.* **170**, 627–641.
80. Schindelin, J., Arganda-Carreras, I., Frise, E., Kaynig, V., Longair, M., Pietzsch, T., Preibisch, S., Rueden, C., Saalfeld, S., Schmid, B., et al. (2012). Fiji: an open-source platform for biological-image analysis. *Nat. Methods* **9**, 676–682.
81. Schneider, C.A., Rasband, W.S., and Eliceiri, K.W. (2012). NIH Image to ImageJ: 25 years of image analysis. *Nat. Methods* **9**, 671–675.
82. Kurihara, D., Mizuta, Y., Sato, Y., and Higashiyama, T. (2015). ClearSee: a rapid optical clearing reagent for whole-plant fluorescence imaging. *Development* **142**, 4168–4179.
83. Ursache, R., Andersen, T.G., Marhavý, P., and Geldner, N. (2018). A protocol for combining fluorescent proteins with histological stains for diverse cell wall components. *Plant J.* **93**, 399–412.
84. Frangi, A.F., Niessen, W.J., Vincken, K.L., and Viergever, M.A. (1998). Multiscale vessel enhancement filtering. In *Medical Image Computing and Computer-Assisted Intervention — MICCAI'98 Lecture Notes in Computer Science*, W.M. Wells, A. Colchester, and S. Delp, eds. (Springer), pp. 130–137.
85. Ollion, J., Cochennec, J., Loll, F., Escudé, C., and Boudier, T. (2013). TANGO: a generic tool for high-throughput 3D image analysis for studying nuclear organization. *Bioinformatics* **29**, 1840–1841.
86. Gul-Mohammed, J., Arganda-Carreras, I., Andrey, P., Galy, V., and Boudier, T. (2014). A generic classification-based method for segmentation of nuclei in 3D images of early embryos. *BMC Bioinformatics* **15**, 9.
87. Bolte, S., and Cordelières, F.P. (2006). A guided tour into subcellular colocalization analysis in light microscopy. *J. Microsc.* **224**, 213–232.

## STAR★METHODS

### KEY RESOURCES TABLE

REAGENT or RESOURCE	SOURCE	IDENTIFIER
<b>Bacterial and Virus Strains</b>		
<i>Pseudomonas protegens</i> CHA0	Stutz et al. <sup>74</sup>	NCBI:txid1124983
<i>Pseudomonas protegens</i> CHA0 - $\Delta$ <i>fliC</i>	This paper	N/A
<i>Pseudomonas protegens</i> CHA0 - $\Delta$ <i>fleQ</i>	Kupferschmied <sup>51</sup>	N/A
<i>Pseudomonas protegens</i> CHA0 – <i>fliC</i> :: <i>pEMG</i>	Kupferschmied <sup>51</sup>	N/A
At-RSPHERE collection: Root 1464	Bai et al. <sup>56</sup>	N/A
At-RSPHERE collection: Root 227	Bai et al. <sup>56</sup>	N/A
At-RSPHERE collection: Root 935 <i>Flavobacterium</i>	Bai et al. <sup>56</sup>	N/A
At-RSPHERE collection: Root 444D2 <i>Paenibacillus</i>	Bai et al. <sup>56</sup>	N/A
At-RSPHERE collection: Root 342 <i>Caulobacter</i>	Bai et al. <sup>56</sup>	N/A
At-RSPHERE collection: Root 700	Bai et al. <sup>56</sup>	N/A
At-RSPHERE collection: Root 105	Bai et al. <sup>56</sup>	N/A
At-RSPHERE collection: Root 1471	Bai et al. <sup>56</sup>	N/A
At-RSPHERE collection: Root 482 <i>Rhizobium</i>	Bai et al. <sup>56</sup>	N/A
At-RSPHERE collection: Root 954 <i>Rhizobium</i>	Bai et al. <sup>56</sup>	N/A
At-RSPHERE collection: Root 142 <i>Sinorhizobium</i>	Bai et al. <sup>56</sup>	N/A
At-RSPHERE collection: Root 50 <i>Sphingomonas</i>	Bai et al. <sup>56</sup>	N/A
At-RSPHERE collection: Root 1294 <i>Sphingomonas</i>	Bai et al. <sup>56</sup>	N/A
At-RSPHERE collection: Root 710 <i>Sphingomonas</i>	Bai et al. <sup>56</sup>	N/A
At-RSPHERE collection: Root 241 <i>Sphingomonas</i>	Bai et al. <sup>56</sup>	N/A
At-RSPHERE collection: Root 1497 <i>Sphingopyxis</i>	Bai et al. <sup>56</sup>	N/A
At-RSPHERE collection: Root 214 <i>Sphingopyxis</i>	Bai et al. <sup>56</sup>	N/A
At-RSPHERE collection: Root 154	Bai et al. <sup>56</sup>	N/A
At-RSPHERE collection: Root 83 <i>Achromobacter</i>	Bai et al. <sup>56</sup>	N/A
At-RSPHERE collection: Root 170 <i>Achromobacter</i>	Bai et al. <sup>56</sup>	N/A
At-RSPHERE collection: Root 565 <i>Achromobacter</i>	Bai et al. <sup>56</sup>	N/A
At-RSPHERE collection: Root 473 <i>Variovorax</i>	Bai et al. <sup>56</sup>	N/A
At-RSPHERE collection: Root 568	Bai et al. <sup>56</sup>	N/A
At-RSPHERE collection: Root 1221	Bai et al. <sup>56</sup>	N/A
At-RSPHERE collection: Root 29	Bai et al. <sup>56</sup>	N/A
At-RSPHERE collection: Root 16D2	Bai et al. <sup>56</sup>	N/A
At-RSPHERE collection: Root 209	Bai et al. <sup>56</sup>	N/A
At-RSPHERE collection: Root 401 <i>Pseudomonas</i>	Bai et al. <sup>56</sup>	N/A
At-RSPHERE collection: Root 562 <i>Pseudomonas</i>	Bai et al. <sup>56</sup>	N/A
At-RSPHERE collection: Root 9 <i>Pseudomonas</i>	Bai et al. <sup>56</sup>	N/A
At-RSPHERE collection: Root 569 <i>Pseudomonas</i>	Bai et al. <sup>56</sup>	N/A
At-RSPHERE collection: Root 68 <i>Pseudomonas</i>	Bai et al. <sup>56</sup>	N/A
At-RSPHERE collection: Root 71 <i>Pseudomonas</i>	Bai et al. <sup>56</sup>	N/A
At-RSPHERE collection: Root 179 <i>Rhodanobacter</i>	Bai et al. <sup>56</sup>	N/A
<b>Chemicals, Peptides, and Recombinant Proteins</b>		
flg22 <sub>Pa</sub>	Peptide Specialty Laboratories GmbH	N/A
flg22 <sub>R569</sub>	Peptide Specialty Laboratories GmbH	N/A
AtPep1	Peptide Specialty Laboratories GmbH	N/A
elf18	Peptide Specialty Laboratories GmbH	N/A
Chitin from shrimp shells	Sigma-Aldrich	Cat#C9752

(Continued on next page)

**Continued**

REAGENT or RESOURCE	SOURCE	IDENTIFIER
(±)-3-Hydroxydecanoic acid (3-OH-C10:0)	Sigma-Aldrich	Cat#H3648
Propidium iodide (PI)	Sigma-Aldrich	Cat#P4170
Piperonylic acid (PA)	Sigma-Aldrich	Cat#P49805
Fluorol Yellow 088	ChemCruz	Cat# sc-215052A
Basic Fuchsin	Sigma-Aldrich	Cat#58969-01-0
Calcofluor White M2R (fluorescent brightener 28)	Polysciences	Cat#4359

**Experimental Models: Organisms/Strains**

<i>Arabidopsis thaliana</i> : WT Col-0	NASC	NCBI:txid3702
<i>Arabidopsis</i> : <i>fls2</i> (SALK)	NASC	SALK_062054C
<i>Arabidopsis</i> : <i>fls2</i> (SAIL)	NASC	SAIL691_C04
<i>Arabidopsis</i> : <i>PER5::NLS-3xmVENUS</i>	Poncini et al. <sup>20</sup>	N/A
<i>Arabidopsis</i> : <i>MYB51::NLS-3xmVENUS</i>	Poncini et al. <sup>20</sup>	N/A
<i>Arabidopsis</i> : <i>FLS2::FLS2-3myc-GFP Ws-0</i>	Robatzek et al. <sup>75</sup>	N/A
<i>Arabidopsis</i> : <i>WER::FLS2-3myc-GFP fls2</i> (SAIL)	Wyrsh et al. <sup>21</sup>	N/A
<i>Arabidopsis</i> : <i>CASP1::FLS2-3myc-GFP fls2</i> (SAIL)	Wyrsh et al. <sup>21</sup>	N/A
<i>Arabidopsis</i> : <i>SHR::FLS2-3myc-GFP fls2</i> (SAIL)	Wyrsh et al. <sup>21</sup>	N/A
<i>Arabidopsis</i> : <i>UBQ10::FLS2-3myc-GFP fls2</i> (SAIL)	Wyrsh et al. <sup>21</sup>	N/A
<i>Arabidopsis</i> : <i>LBD16::FLS2-3myc-GFP fls2</i> (SAIL)	Wyrsh et al. <sup>21</sup>	N/A
<i>Arabidopsis</i> : <i>RCH1::FLS2-3myc-GFP fls2</i> (SALK)	This paper	N/A
<i>Arabidopsis</i> : <i>PRP3::FLS2-3myc-GFP fls2</i> (SALK)	This paper	N/A
<i>Arabidopsis</i> : <i>GRP::FLS2-3myc-GFP fls2</i> (SALK)	This paper	N/A
<i>Arabidopsis</i> : <i>PER5::NLS-3xmVENUS WER::FLS2-3myc-GFP fls2</i> (SAIL)	This paper	N/A
<i>Arabidopsis</i> : <i>PER5::NLS-3xmVENUS CASP1::FLS2-3myc-GFP fls2</i> (SAIL)	This paper	N/A
<i>Arabidopsis</i> : <i>PER5::NLS-3xmVENUS SHR::FLS2-3myc-GFP fls2</i> (SAIL)	This paper	N/A
<i>Arabidopsis</i> : <i>PER5::NLS-3xmVENUS UBQ10::FLS2-3myc-GFP fls2</i> (SAIL)	This paper	N/A
<i>Arabidopsis</i> : <i>PER5::NLS-3xmVENUS fls2</i> (SAIL)	This paper	N/A
<i>Arabidopsis</i> : <i>PER5::NLS-3xmVENUS RCH1::FLS2-3myc-GFP fls2</i> (SALK)	This paper	N/A
<i>Arabidopsis</i> : <i>PER5::NLS-3xmVENUS PRP3::FLS2-3myc-GFP fls2</i> (SALK)	This paper	N/A
<i>Arabidopsis</i> : <i>PER5::NLS-3xmVENUS GRP::FLS2-3myc-GFP fls2</i> (SALK)	This paper	N/A
<i>Arabidopsis</i> : <i>MYB51::NLS-3xmVENUS WER::FLS2-3myc-GFP fls2</i> (SAIL)	This paper	N/A
<i>Arabidopsis</i> : <i>MYB51::NLS-3xmVENUS CASP1::FLS2-3myc-GFP fls2</i> (SAIL)	This paper	N/A
<i>Arabidopsis</i> : <i>MYB51::NLS-3xmVENUS SHR::FLS2-3myc-GFP fls2</i> (SAIL)	This paper	N/A
<i>Arabidopsis</i> : <i>MYB51::NLS-3xmVENUS UBQ10::FLS2-3myc-GFP fls2</i> (SAIL)	This paper	N/A
<i>Arabidopsis</i> : <i>MYB51::NLS-3xmVENUS GFP fls2</i> (SAIL)	This paper	N/A
<i>Arabidopsis</i> : <i>UBQ10::NLS-mTurquoise2 PER5::NLS-3xmVENUS WER::FLS2-3myc-GFP fls2</i> (SAIL)	This paper	N/A
<i>Arabidopsis</i> : <i>UBQ10::NLS-mTurquoise2 PER5::NLS-3xmVENUS CASP1::FLS2-3myc-GFP fls2</i> (SAIL)	This paper	N/A

(Continued on next page)

**Continued**

REAGENT or RESOURCE	SOURCE	IDENTIFIER
<i>Arabidopsis</i> : UBQ10::NLS-mTurquoise2 PER5::NLS-3xmVENUS SHR::FLS2-3myc-GFP fls2 (SAIL)	This paper	N/A
<i>Arabidopsis</i> : UBQ10::NLS-mTurquoise2 PER5::NLS-3xmVENUS UBQ10::FLS2-3myc-GFP fls2 (SAIL)	This paper	N/A
<i>Arabidopsis</i> : UBQ10::NLS-mTurquoise2 PER5::NLS-3xmVENUS fls2 (SAIL)	This paper	N/A
<i>Arabidopsis</i> : UBQ10::NLS-mTurquoise2 MYB51::NLS-3xmVENUS WER::FLS2-3myc-GFP fls2 (SAIL)	This paper	N/A
<i>Arabidopsis</i> : UBQ10::NLS-mTurquoise2 MYB51::NLS-3xmVENUS CASP1::FLS2-3myc- GFP fls2 (SAIL)	This paper	N/A
<i>Arabidopsis</i> : UBQ10::NLS-mTurquoise2 MYB51::NLS-3xmVENUS SHR::FLS2-3myc-GFP fls2 (SAIL)	This paper	N/A
<i>Arabidopsis</i> : UBQ10::NLS-mTurquoise2 MYB51::NLS-3xmVENUS UBQ10::FLS2-3myc- GFP fls2 (SAIL)	This paper	N/A
<i>Arabidopsis</i> : UBQ10::NLS-mTurquoise2re MYB51::NLS-3xmVENUS fls2 (SAIL)	This paper	N/A
<i>Arabidopsis</i> : UBQ10::NLS-tdTomato PER5::NLS- 3xmVENUS	This paper	N/A
<i>Arabidopsis</i> : UBQ10::NLS-tdTomato MYB51::NLS-3xmVENUS	This paper	N/A
<i>Arabidopsis</i> : UBQ10::R-GECO1	Keinath et al. <sup>26</sup>	N/A
<i>Arabidopsis</i> : UBQ10::R-GECO1 fls2 (SAIL)	This paper	N/A
<i>Arabidopsis</i> : UBQ10::R-GECO1 WER::FLS2- 3myc-GFP fls2 (SAIL)	This paper	N/A
<i>Arabidopsis</i> : UBQ10::R-GECO1 CASP1::FLS2- 3myc-GFP fls2 (SAIL)	This paper	N/A
<i>Arabidopsis</i> : UBQ10::R-GECO1 SHR::FLS2-3myc- GFP fls2 (SAIL)	This paper	N/A
<i>Arabidopsis</i> : UBQ10::R-GECO1 UBQ10::FLS2- 3myc-GFP fls2 (SAIL)	This paper	N/A
<b>Oligonucleotides</b>		
Primer for ΔfliC, ΔfleQ and fliC::pEMG generation: see Table S3	Kupferschmied <sup>51</sup> , this paper	N/A
<b>Recombinant DNA</b>		
UBQ10::NLS-mTurquoise2	This paper	N/A
UBQ10::NLS-tdTomato	This paper	N/A
RCH1::FLS2-GFP	This paper	N/A
PRP3::FLS2-GFP	This paper	N/A
GRP::FLS2-GFP	This paper	N/A
pEMG	Martínez-García and de Lorenzo <sup>76</sup>	NCBI: JF965437.1
pSW-2	Martínez-García and de Lorenzo <sup>76</sup>	N/A
pME8323	Kupferschmied <sup>51</sup>	N/A
pME11121	This paper	N/A
<b>Software and Algorithms</b>		
Fiji (ImageJ)	Schneider et al. <sup>77</sup>	<a href="https://imagej.nih.gov/ij/">https://imagej.nih.gov/ij/</a>
Graphpad Prism 7.0	GraphPad Software	<a href="https://www.graphpad.com/">https://www.graphpad.com/</a>
R3.6.0	R Core Team (2013)	<a href="http://www.R-project.org/">http://www.R-project.org/</a>

## RESOURCE AVAILABILITY

### Lead Contact

Further information and requests for resources and reagents should be directed to and will be fulfilled by the Lead Contact, Niko Geldner ([niko.geldner@unil.ch](mailto:niko.geldner@unil.ch)).

### Materials Availability

Plasmids and transgenic plant seeds generated in this study will be made available on request, but we may require a payment and/or a completed Materials Transfer Agreement if there is potential for commercial application.

### Data and Code Availability

This study did not generate datasets or code.

## EXPERIMENTAL MODEL AND SUBJECT DETAILS

### Plant material

*Arabidopsis thaliana* ecotype Columbia Col-0 was used for most experiments. The T-DNA lines *fls2* were obtained from NASC (SAIL691\_C04 and SALK\_062054C) and originally described in Zipfel et al.<sup>7</sup>. The recombinant *WER::FLS2-3myc-GFP*, *CASP1::FLS2-3myc-GFP*, *SHR::FLS2-3myc-GFP*, *UBQ10::FLS2-3myc-GFP*, *LBD16::FLS2-3myc-GFP* in *fls2* (SAIL691\_C04) background, as well as *FLS2::FLS2-3myc-GFP* in Wassilewskija Ws-0 background were provided by Prof. Thomas Boller's group<sup>21,75</sup>. The defense marker lines *PER5::NLS-3mVenus* and *MYB51::NLS-3mVenus* are described in<sup>20</sup>. Calcium signaling analysis was carried out thanks to the line *UBQ10::R-GECO1* kindly shared by Prof. Melanie Krebs's group<sup>26</sup>.

*PER5::NLS-3mVenus* and *MYB51::NLS-3mVenus* lines were crossed to the four recombinant lines *WER::*, *CASP1::*, *SHR::* and *UBQ10::FLS2-3myc-GFP fls2* lines as well as to the *fls2* (SAIL691\_C04) mutant. In addition, *UBQ10::R-GECO1* was first crossed to *fls2* (SAIL691\_C04) mutant, then the resulting homozygous line was crossed again to the four recombinant lines (*WER::/CASP1::/SHR::/UBQ10::FLS2-3myc-GFP fls2* (SAIL691\_C04)), so that F1 could be directly used for experiments. For quantification of tissue-specific nuclear signal, the constructs *UBQ10::NLS-mTurquoise2* or *UBQ10::NLS-tdTomato* were transformed by floral dipping method in all *PER5::/MYB51::NLS-3mVenus* marked *prom::FLS2-3myc-GFP fls2* (SAIL691\_C04), *fls2* (SAIL691\_C04) and wild-type lines<sup>78</sup>. In addition, *RCH1::FLS2-GFP*, *PRP3::FLS2-GFP* and *GRP::FLS2-GFP* were transformed in *fls2* (SALK\_062054C).

### Plant growth conditions

For all experiments, seeds were surface-sterilized by gaseous chlorine for 2.5 hours or immersed in a solution of 70% EtOH 0.01% Triton X-100 for 5 min, washed once in 96% EtOH and dried under sterile conditions. Seeds were stratified in the obscurity for two days, then germinated on 1% agar plates containing half-strength Murashige and Skoog (½ MS) medium and 500mg/l MES (Duchefa). Seedlings were grown vertically for 5 days before analysis (otherwise differently specified) in continuous light at 23°C.

For experiments done in Cologne, seeds were sown on 1% Bacto-Agar supplemented with ½ MS with 250mg/l of MES. Seedlings were grown in a light cabinet with short day conditions (10h light-14h dark, 21°/19°C, 65% relative humidity).

### Bacterial strains and growth conditions

*Pseudomonas protegens* strain CHA0 used in this study is a tobacco root isolate with plant-beneficial activities<sup>74</sup>. CHA0 mutants  $\Delta fliC$  and  $\Delta fleQ$  carrying in-frame deletions in the *fliC* and *fleQ* genes, respectively, were generated using the suicide vector pEMG and the I-SceI system<sup>51,76</sup> adapted to *P. protegens*<sup>79</sup> with plasmids and primers listed in Table S3. Insertional mutant *fliC::-pEMG* was generated with the same method. The *Pseudomonas* R569 and other natural commensal bacterial isolates were obtained from the At-SPHERE culture collection<sup>56</sup>. CHA0 strains and commensal isolates were routinely cultured at 28°C in half-strength tryptic soy broth (TSB) (Sigma-Aldrich).

## METHOD DETAILS

### Plant plasmid construction

Generation of expression constructs was performed with both In-Fusion Advantage PCR Cloning Kit (Clontech) and Gateway Cloning Technology (Invitrogen).

For nuclei labeling with blue fluorochrome, used for quantification, *UBQ10::NLS-mTurquoise2* was generated by triple Gateway recombination reaction using the entry clones pDONR P4-*pUBQ10-P1R*<sup>13</sup>, pDONR P1-*NLS-mTurquoise2-P2* and pDONR P2R-*2R3e-nosT-P3*<sup>80</sup> with the destination vector pK7m34GW,0 containing a kanamycin resistance gene for plant selection. For the red version of nuclei labeling, the plasmid *UBQ10::NLS-tdTomato* was used for its FastRed *in plantae* selection system. Briefly, pDONR P4-*pUBQ10-P1R*<sup>13</sup> and pDONR P1-*NLS-tdTomato-P2* were combined with the destination vector pFR7m24GW by double Gateway reaction. pDONR P1-*NLS-tdTomato-P2* was previously generated using in-Fusion cloning to integrate the NLS sequence to pDONR P1-*tdTomato-P2*.

*RCH1::FLS2-GFP*, *PRP3::FLS2-GFP* and *GRP::FLS2-GFP* were generated combining the respective entry clones pDONR L4-*pRCH1-R1* and L4-*pPRP3-R1* (SWELL lines)<sup>36</sup>, or pDONR L4-*pGRP-R1*<sup>49</sup>, with pDon207 containing the L1-*FLS2-3xmyc-GFP-L2* sequence<sup>21</sup>, in the destination clone pH7m24GW,3.

### Elicitors and inhibitors treatments

Commercial flg22<sub>Pa</sub> peptide from *Pseudomonas aeruginosa* (QRLSTGSRINSKDDAAGLQIA) was ordered from EZBioLab. Elf18 oligopeptide from *Escherichia coli* strain G1826 (Ac-SKEKFERTKPHVNVGTIG), *A. thaliana* Plant Elicitor Peptide 1, AtPEP1 (ATKV-KAKQRGKEKVSSGRPGQHN) and flg22<sub>R569</sub> peptide (NRLSTGKKNINSKDDAAGMQIA) from the isolate *Pseudomonas* R569 were synthesized by Peptide Specialty Laboratories GmbH. (±)-3-Hydroxydecanoic acid (3-OH-C10:0) and chitin were obtained from Sigma-Aldrich. All elicitors were dissolved in deionized MilliQ sterile water at the respective stock concentration of 1mM for flg22<sub>Pa</sub>, flg22<sub>R569</sub>, elf18, AtPep1 and 3-OH-C10:0; and 2mg/ml for chitin. For the inhibition of monolignol synthesis, piperonylic acid (PA, Sigma-Aldrich) was dissolved in absolute EtOH at a concentration of 20mM for stock solution.

For elicitor treatments, chemicals were diluted in liquid half strength MS medium (½ MS) to the indicated concentration. Seedlings were grown vertically for 4 days on small ½ MS Petri dishes (5.5cm diameter), then 1.5ml of elicitor solution was gently poured over the seedlings to avoid damages induced by transfer. Care was taken that all roots were properly submerged. Seedlings were incubated horizontally for 24h before live imaging of 5-day-old plants or fixation. Cell wall of living samples were stained with 15mM (10 mg/ml) propidium iodide (PI). For Figure 4A, 4-day-old seedlings were carefully transferred into a Chambered Coverglass (Nunc Lab-Tek, 2-well format, Thermo Scientific) and roots covered with a block of solid half MS, previously stained by propidium iodide (100 µL of 100 mg/ml PI solution infused in 1ml solid half MS volume). Chambers were closed and mounted onto confocal. After the first imaging time point at 0h, 300 µL of 5 µM flg22 solution was added on top of the block of agar and let diffused overnight. Imaging at time point 14h was performed after removal of excess solution.

For root growth analysis, 5day-old seedlings were carefully transferred on new ½ MS agar plates containing 1 µM flg22<sub>Pa</sub> or flg22<sub>R569</sub> and grown vertically for 6 days in standard growth conditions.

For combined treatment with PA and flg22, Col-0 and *WER::FLS2* seedlings were grown for 4 days on ½ MS plates, then were transferred on agar plates supplemented with 10 µM PA or ethanol as control. To overcome PA degradation by light but to still conserve proper root growth in control conditions, plates were inserted in black boxes open to the top, allowing roots to grow in the obscurity but leaves to reach the light. Roots were hidden from top light using black sterile plastic caches. After overnight pre-treatment, seedlings were again transferred on plates containing 10 µM PA/EtOH with/without 1 µM flg22/mock, using the same black boxes. Their root tip location was recorded. 48h after the first transfer, root growth was measured, and seedlings were fixed as described.

### Microscopy settings and image processing

Imaging was performed on either a Zeiss LSM880, LSM700 or a Leica SP8 inverted confocal scanning microscope. Pictures were taken with a 63x oil immersion objective (Zeiss LSM880), 63x water immersion objective (Leica SP8), 40x water immersion objective (Leica SP8), as well as 20x or 10x dry immersion objectives for tile-scan with 10% overlap (Zeiss LSM880 or LSM700).

The excitation and detection windows were set as following: for visualization of FLS2 and defense markers, on Leica SP8, GFP/PI (488nm, 500-530nm and 600-670nm); GFP/mVenus/PI (488nm, 490-508nm; 514nm, 517-560nm and 600-670nm, sequential scan), on Zeiss LSM880, GFP/PI(488nm, 500-530nm and 600-650nm respectively), mVenus (514nm, 520-550nm). For lignin analysis: on Zeiss LSM880, calcofluor (405nm, 425-475nm), basic fuchsin (561nm, 600-650nm). For cell-specific quantification: on Zeiss LSM880, DirectRed 23/mVenus/mTurquoise2 (561nm, 580-700nm; 514nm, 520-590nm; 458nm, 460-500nm; sequential scan) and Calcofluor/mVenus/tdTomato (405nm, 415-450nm; 514nm, 520-545nm; 561nm; 570-640nm, sequential scan). For calcium analysis: Zeiss LSM880, R-GECO1 (561 nm, 580-640nm). For suberin staining: on Zeiss LSM700, fluorol yellow (488nm, 500-600nm).

Images were processed using the Fiji software<sup>81,77</sup>. For cross-section maximum projection of MAMP-induced signal (Figures 2B, 2C, 3B, and 3C), z stack pictures were resliced then realigned thanks to the Descriptor-based series registration (2d/3d + t) plugin. A maximum projection of the MAMP marker channel was then merged to a representative single stack of the PI-stained cell wall channel.

### Fixation and staining

Fixation and cell-wall staining were performed according to adapted Clearsee protocol<sup>82,83</sup>. Briefly, 5-day-old seedlings were fixed for 1h at room temperature under vacuum in 4% paraformaldehyde PBS solution, using 6-well plates, then washed twice for 1min with PBS. Once fixed, seedlings were cleared in Clearsee solution for at least 24h under mild shaking. To visualize cell wall for quantification, clearing solution was exchanged with either 0.1% Calcofluor White or 0.1% Direct Red 23 in Clearsee solution. After at least respectively 30min and 2h of staining, the staining solution was removed and samples rinsed once in fresh Clearsee solution, then washed for 30min in a renewed Clearsee solution with gentle shaking before mounting.

For combined cell wall and lignin staining, fixed and cleared samples were incubated overnight in a Clearsee solution supplemented with 0.2% Basic Fuchsin and 0.1% Calcofluor White. Once the dye solution removed, samples were rinsed once, washed first 30min then at least 1.5h before observation.

### Ca<sup>2+</sup> imaging on roots

For calcium responses analysis, *UBQ10::R-GECO1* samples were mounted as follows. Seedlings, once at a time, were glued to a large (60mm) coverslip previously sprayed with medical adhesive (Adapt Medical Adhesive Spray, Hollister). A silicon isolator (Grace

Bio-Labs Press-to-seal silicon isolator, No PSA, 20mm diameter, Sigma) was then quickly placed around the seedling and 600 $\mu$ L of sterile germination medium (0.75mM CaCl<sub>2</sub>, 1mM KCl, 0.25mM Ca(NO<sub>3</sub>)<sub>2</sub>·4H<sub>2</sub>O, 1mM MgSO<sub>4</sub>·7H<sub>2</sub>O, 0.2mM KH<sub>2</sub>PO<sub>4</sub>, 50  $\mu$ M NaFe(III) EDTA, 50  $\mu$ M H<sub>3</sub>BO<sub>3</sub>, 5  $\mu$ M MnCl<sub>2</sub>·4H<sub>2</sub>O, 10  $\mu$ M ZnSO<sub>4</sub>·7H<sub>2</sub>O, 0.5  $\mu$ M CuSO<sub>4</sub>·5H<sub>2</sub>O, 0.1  $\mu$ M Na<sub>2</sub>MoO<sub>3</sub>, pH adjusted to 5.6 with NaOH) was dropped on the root. The drop was spread with a pipet tip to cover the whole surface delimited by the silicon isolator and the seedling let to rest for at least 20min. For full root imaging, tile scans combined to time laps were performed under Zeiss LSM880 confocal laser scanning microscope with 20x objective as described above. As few tiles as possible were selected to limit time acquisition, no averaging was done, and the pinhole was entirely open. Images were taken continuously, with an average time interval of 5 to 7 s. Acquisition of baseline signal was performed for 5min, then 7.5  $\mu$ L of 100  $\mu$ M flg22 diluted in water was added to the germination medium solution. Acquisition was continued for at least 20min (Video S1). For tissue-specific imaging and quantification, small z stack (~8 slices) with 5  $\mu$ m intervals were taken on half a root in the elongation zone for wild-type, *fls2* (SAIL691\_C04) and *WER::FLS2* samples, or in the differentiated zone for *CASP1::SHR::UBQ10::FLS2* (Video S2).

### Suberin staining

To highlight suberin lamellae, seedlings were fixed and stained with the methanol-based fluorol yellow staining protocol as described in Fujita et al.<sup>67</sup>. Briefly, treated 5-day-old seedlings were incubated in methanol for three days at room temperature. The cleared samples were then transferred to a fresh solution of 0.01% Fluorol Yellow 088 (in methanol) and incubated for 1h. After staining, seedlings were rinsed shortly in methanol and transferred to a new solution of 0.5% aniline blue (in methanol) for counterstaining. Finally, samples were washed for 2–3min in water and transferred to a chambered coverglass (Thermo Scientific), covered with a piece of 1% half-strength MS agar. Seedling were imaged using tile-scan on the Zeiss LSM700 as described above.

### Bacterial root inoculation assays

PTI assays and lignin analyses were performed after drop inoculation on agar plates. Briefly, 2  $\mu$ L of bacterial suspension (cells centrifuged and resuspended in fresh 50% TSB) of OD<sub>600</sub> = 0.01 was added to the tip of 5-day-old seedlings. Once the drop dried, seedlings were grown vertically in standard conditions for 1 to 3 days. For the fast screening of bacterial isolates, roots were observed under a Leica DM 5500B epifluorescence microscope (GFP lamp). Representative pictures of roots were imaged using confocal scanning microscopy (Leica SP8) after a short wash in deionized H<sub>2</sub>O.

Root growth inhibition assays were completed on agar plates inoculated with bacteria at mentioned concentrations. Briefly, bacterial cultures were grown as previously described in 50% TSB, then centrifuged and resuspended in fresh medium. OD<sub>600</sub> was measured and adjusted to 100x the desired concentration. 500  $\mu$ L of concentrated bacterial inoculum was then added to 50ml of semi solid 1/2 MS medium afore cooled down to around 30°C. Inoculated media were gently mixed by inverting several times, then poured in square Petri dishes. Five-day-old *WER::FLS2* and wild-type Col-0 seedlings previously grown on mesh (15mm x 100mm, on top of the plate), were transferred with sterile forceps on the inoculated plates. Seedlings were selected for similar root size, the ones being obviously too long or too short removed from the mesh with sterile toothpicks. After transfer, root tip locations were marked for keeping track of growth, then plants were grown in standard conditions for 6 days. One day post-inoculation, root tip positions were again recorded, and all seedlings that completely stopped to grow were dismissed from the analysis. This ensured that only seedlings that recovered properly from the transfers were considered. Plates were scanned at 6dpi and root growth measured using Fiji plugins “Simple Neurite Tracer”<sup>84</sup>.

### CFU counting

Four-day-old seedlings were inoculated with the drop-inoculation method described above. One day-post inoculation, seedlings were imaged, then harvested, gently washed by dipping in sterile deionized water, dried on sterile filter paper and collected in sterile Eppendorfs containing 500  $\mu$ L of extraction buffer (10mM MgCl<sub>2</sub>, 0.01% Silwet L-77). Three seedlings were pooled together for each of the three technical replicates. Seedlings were homogenized using TissueLyser II (QIAGEN, Germany) with stainless steel beads. Samples were diluted in series with 10-folds steps, then 20  $\mu$ L of each concentration was spotted on LB agar plates. CFU were counted for the most appropriate dilution (final dilution: 4'000 or 10'000-fold) after 24h incubation at 28°C until colonies are clearly visible. Calculated number of total CFU was normalized by centimeter of root length measured from images ((CFU/ml x 500/3)/mean Root Length). The experiment was conducted in three biological replicates. All data were finally pooled together.

### Swimming assay

Overnight culture of CHA0 and  $\Delta$ *fliC*,  $\Delta$ *fliQ* and *fliC::pEMG* was adjusted to OD<sub>600</sub> = 0.1. Ten microliters of this bacterial suspension were spotted at the center of a NA plate. Bacterial motility was observed after 24 hours of incubation at 25°C.

## QUANTIFICATION AND STATISTICAL ANALYSIS

### Cell-specific quantification

To realize the complete atlas of defense marker responses, the different *prom::FLS2* lines analyzed were first transformed with *UBQ10::nls-mTurquoise2* to delimit nuclei. Alternatively, wild-type *PER5::* and *MYB51::NLS-3Venus* lines were transformed with *UBQ10::nls-tdTomato*, which comprise a FastRed rather than a Kanamycin selection. This allowed to quantify directly the T1 and skip one generation. After flg22 treatment, seedlings were fixed in Clearsee and their cell wall stained with DirectRed23, or Calcofluor

White respectively. Z stack were imaged on half section of the roots at 4 different positions, i.e., meristematic zone (MZ), elongation zone (EZ), 12 cells and 30 cells after the onset of elongation for 3 to 6 roots by treatment (mock and flg22) and by genotype. Three channels were acquired sequentially for the nuclei (*mTurquoise2* or *tdTomato*), the cell wall (DirectRed23 or Calcofluor White) and the defense markers *PER5* and *MYB51* (mVenus), using the same settings on all pictures for mVenus channel. However, wild-type *UBQ10::NLS-tdTomato* and *prom::FLS2 UBQ10::NLS-mTurquoise2* were imaged with distinct settings due to difference of intensity of the nuclei-labeling constructs. Pictures were processed on Fiji software with a custom batch macro automatizing the following pipeline<sup>77</sup>. Images were first resliced from the top, then the three channels were separated. A Gaussian blur was applied on the nuclear and cell wall marker channels, while the PTI marker channel was left untouched to not affect the signal to measure. In a second step, the cell wall channel was subtracted to the nuclear channel to reduce the unspecific background noise of the *UBQ10::nls-mTurquoise2* marker. The “cleaned” nuclear marker channel was transform to 8 bits to facilitate further processing.

We then used the 3D suite to generate a 3-dimensional Region Of Interest (ROI) for each nucleus<sup>85</sup>. We first applied the plugin 3D iterative thresholding on the 8bits-cleaned-nuclear marker channel<sup>86</sup>. In this process, all possible thresholds are tested, which will detect objects for all thresholds. Subsequently, the algorithm will define the best object segmentation for each of the object, which means that different objects can be segmented with different threshold. This is particularly useful to detect objects with variable intensity in an uneven background, to which a single intensity threshold would either miss many objects or include background noise. We used the following settings: min vol pix = 250, max vol pix = 10000, min threshold = 0, min contrast (exp) = 5, criteria method = COMPACTNESS, threshold method = STEP, Segment results = All, value method = 10.0, Starts at mean = on. The plugin gives as output the 3D threshold delimiting all the future ROIs, i.e., the nuclei to quantify. It must be noted that depending on the pictures, some nuclei can be missed, or false positive can be added, but all pictures were then manually curated in a later step. The output came as 2-channels-images, whose last channel is completely black and can be removed by the splitting channel function.

We then use the 3D object counter plugin to define all ROIs, based on the 3D threshold obtained previously, and to redirect the analysis on the defense marker channel<sup>87</sup>. Options were set using the 3D OC Options as following: all parameters were selected, i.e., “Volume,” “Nb of Obj. voxels,” “Nb of Surf. voxels,” “Integrated Density,” “Mean Gray Value,” “Std Dev Gray Value,” “Median Gray Value,” “Minimum Gray Value,” “Maximum Gray Value,” “Centroid” “Mean distance to surface,” “Std Dev distance to surface,” “Median distance to surface,” “Centre of mass,” and “Bounding box.” In addition, we ticked both parameters “Close original images while processing” and “Show masked image. The maps’ parameters were set as follows: dots size = 5, font size = 12, “Show numbers” and “White numbers” were ticked. Importantly, the “Results Table Parameters” should be set on: “Store results within a table named after the image,” which allows to keep track of the files in batch mode. Finally, the measures were “Redirected to” the defense marker channel. After setting all the parameters, the analyze “3D Object Counter” was run. Threshold was set to 1 and minimum size filter to 10. The following maps and result tables were asked to be shown: objects, centroids, statistics, summary.

The process gives in output four different files. The “Centroid map” shows the center of each ROI by a dot, numbered accordingly. The “Object map” is the representation of all ROIs, each of them being numbered. Our macro merges this map to both the cell wall marker channel and the nuclei channel for later identification of nuclei. The 3D Object counter also provides a .csv file called “Statistics” with all parameters measured for each nucleus. The last file provided is the “Masked image,” which represent the defense marker channel masked by the threshold.

To terminate the quantification, each dataset was manually curated to assign a tissue (epidermis, cortex, endodermis, stele or root cap) to each nucleus. A maximum of around 20 nuclei by tissue type and by picture were identified. “Mean Gray Values” was extracted and use for analysis. Mean nuclear intensity for each genotype, treatment, root region and tissue were calculated and color coded using the heatmaply() function in R (heatmaply library). Atlas maps were drawn according to these colored values. Fold changes for *MYB51* induction were calculated and color-coded using the same procedure.

### Calcium signaling quantification

R-GECO1 signal was quantified for each tissue on the z stack acquisition. ROIs delimiting a tissue type were drawn manually on the most appropriate stack (i.e., that presents a clear surface view if possible), using maximum projection of two stacks when necessary.

Fractional fluorescence changes  $\Delta F/F$  were calculated for each ROI from background corrected intensity values as  $(F-F_0)/F_0$ , where  $F_0$  is equal to the average fluorescent intensity of the baseline of the measure, on 4min from  $t = 0$ .

### Statistical analysis

Statistical analyses were done using R3.6.0 (<http://www.R-project.org/>) or Graphpad Prism 7.0 software (<https://www.graphpad.com/>). For multiple comparison, ANOVA followed by Tukey’s Honestly Significant difference (HSD) test were applied when linear model assumptions were met. On the contrary, Kruskal-Wallis test followed by Dunn’s multiple comparison test were performed. For analysis of suberization along the roots, comparisons were performed for each zone separately, and different letters indicates significant differences for a given zone (a, b, c or a’, b’, c’ or a”, b”, c”). Multiple comparison for cell-specific quantifications used Kruskal-Wallis test followed by Pairwise Wilcoxon Rank Sum Tests (p value adjusted with Benjamini-Hochberg). Statistical parameters are reported in figures.

**Current Biology, Volume 31**

**Supplemental Information**

**Spatially Restricted Immune Responses**

**Are Required for Maintaining Root**

**Meristematic Activity upon Detection of Bacteria**

**Aurélia Emonet, Feng Zhou, Jordan Vacheron, Clara Margot Heiman, Valérie Dénervaud Tendon, Ka-Wai Ma, Paul Schulze-Lefert, Christoph Keel, and Niko Geldner**

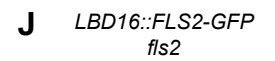
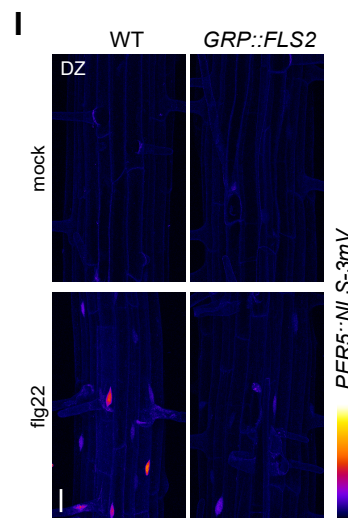
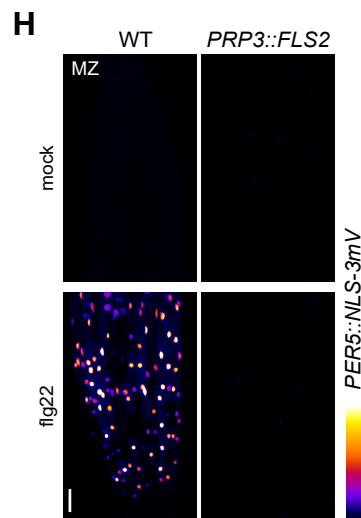
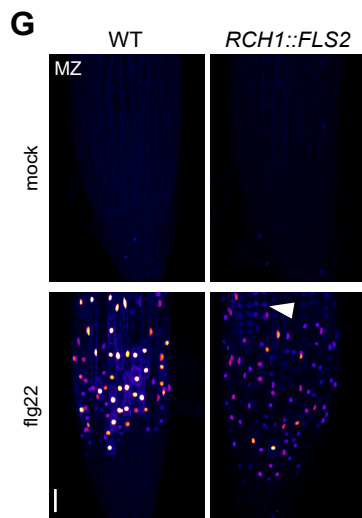
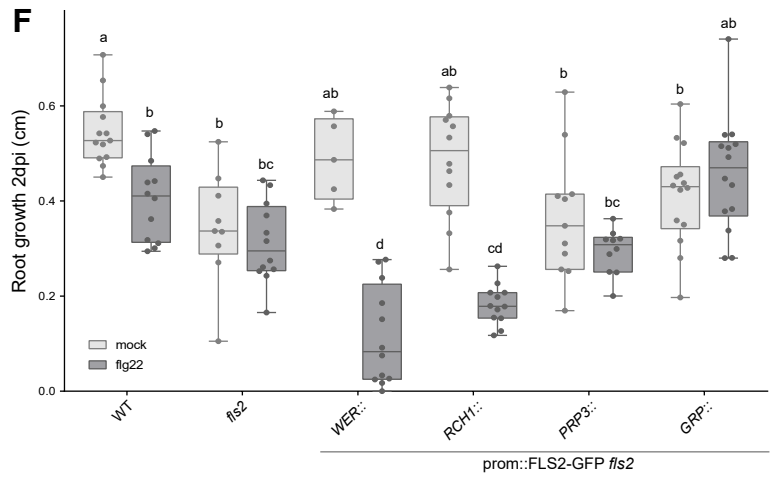
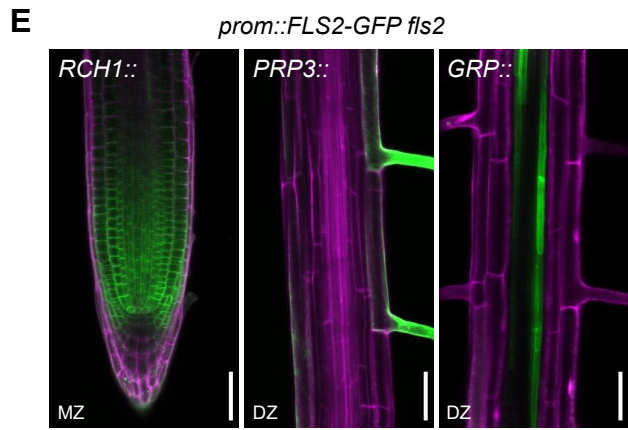
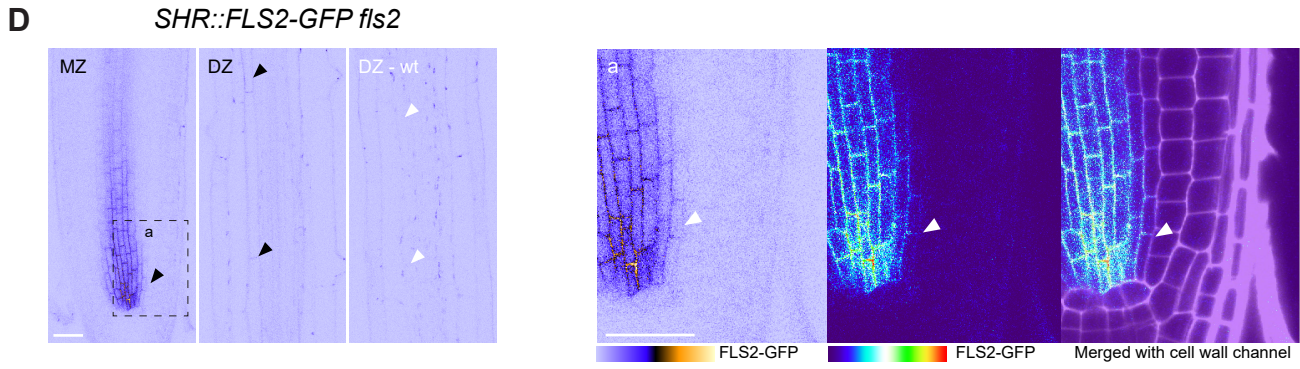
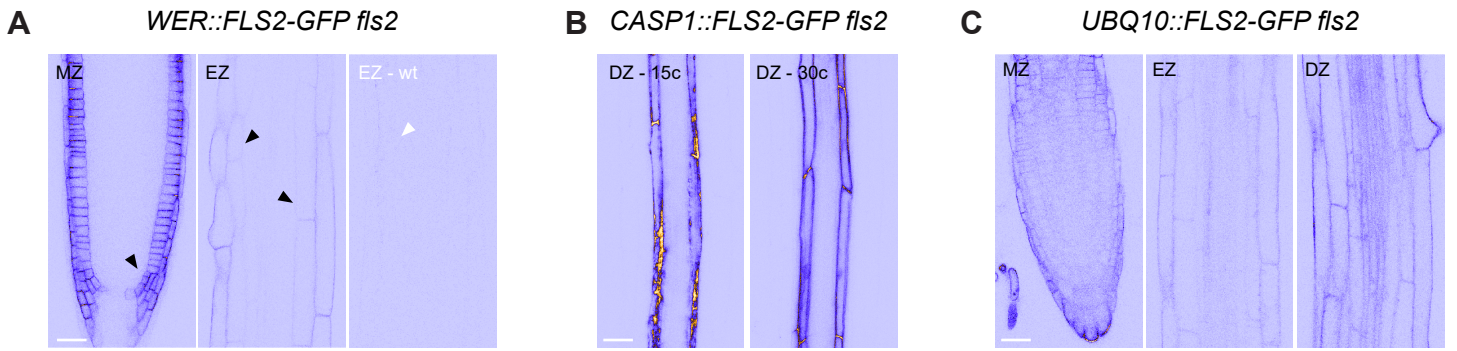


**Figure S1: Expression pattern of *prom::FLS2* complementing *fls2*, related to Figure 1**

**(A)** *WER::FLS2-GFP* expression. *WER* promoter expressed principally *FLS2* in epidermal cells, but some weak signal can be observed in cortex (black arrowheads). Picture of wild-type plants taken with identical setting (EZ-wt) is showed for comparison (cortical cell, white arrowhead). **(B)** *CASP1::FLS2-GFP* is expressed exclusively in endodermal cell line in early and later differentiated zones (15 cells respectively 30 cells after onset of elongation). **(C)** *UBQ10::FLS2-GFP* is expressed in all tissue types in every region of the root. **(D)** *SHR::FLS2-GFP* is expressed strongly in the stele of the meristem then decreases in intensity in later regions. Some weak signal can be detected in endodermal cells (black arrowheads). Picture of wild-type plants taken with identical setting (DZ-wt) is shown for comparison (endodermal cells, white arrowheads). Close-up view of dashed squared box is found in (a). *FLS2-GFP* (visualized by ICA and Thermal LUTs) is merged with cell wall stained by PI (white). White arrowheads point at endodermal cells expressing weakly *FLS2*. Representative pictures are presented. Nine to twelve seedlings over 3 to 4 independent biological replicates were analysed for each genotype for (A) to (D). **(E)** *RCH1* promoter expresses *FLS2* in the meristem, *PRP3::* in the root hair cells and *GRP::* in the pericycle cells in *fls2* (SALK\_062054C). *FLS2-GFP* (green) is co-visualized with PI-stained cell wall (magenta). Representative pictures taken from the analysis of 3 to 6 seedlings from twelve independent lines over two replicates. **(F)** Flg22 treatment increases root growth inhibition in *WER::* and *RCH1::FLS2-GFP fls2* (SAIL691\_C04 and SALK\_062054C, respectively) hypersensitive line only. Root length quantification of *prom::FLS2-GFP fls2* lines treated with 1 $\mu$ M flg22 for 2 days compared to WT (Col-0 background) and *fls2* (SALK\_062054C) mutant. Boxplot centre represents the median (5  $\leq$  n  $\leq$  14). Different letters indicate statistically significant difference between means by 2-ways ANOVA and Tukey's multiple comparison. **(G-I)** Maximal projection *PER5::NLS-3mVenus* marker (Fire LUT) in *RCH1::FLS2-GFP fls2* (G), *PRP3::FLS2-GFP fls2* (H) and *GRP::FLS2-GFP fls2* (I) compared to WT (Col-0 background) shown for MZ (G and H) or DZ (I). For (G) to (H), seedlings were treated for 24h with 1 $\mu$ M flg22. White arrow, epidermal signal. Images were taken with identical settings. Representative pictures are presented. Six to nine seedlings over 2 independent biological replicates were analysed for each genotype. **(J)** *LBD16* promoter expresses *FLS2-GFP* in all tissues in the differentiated zone (DZ). Note that in contrast to previous report, *FLS2* is present in epidermis, cortex and endodermis (white arrows) in addition to the stele. Representative picture taken from the analysis of 8 seedlings. Meristematic zone (MZ), elongation zone (EZ), differentiation zone (DZ). Scale bar, 25 $\mu$ m.

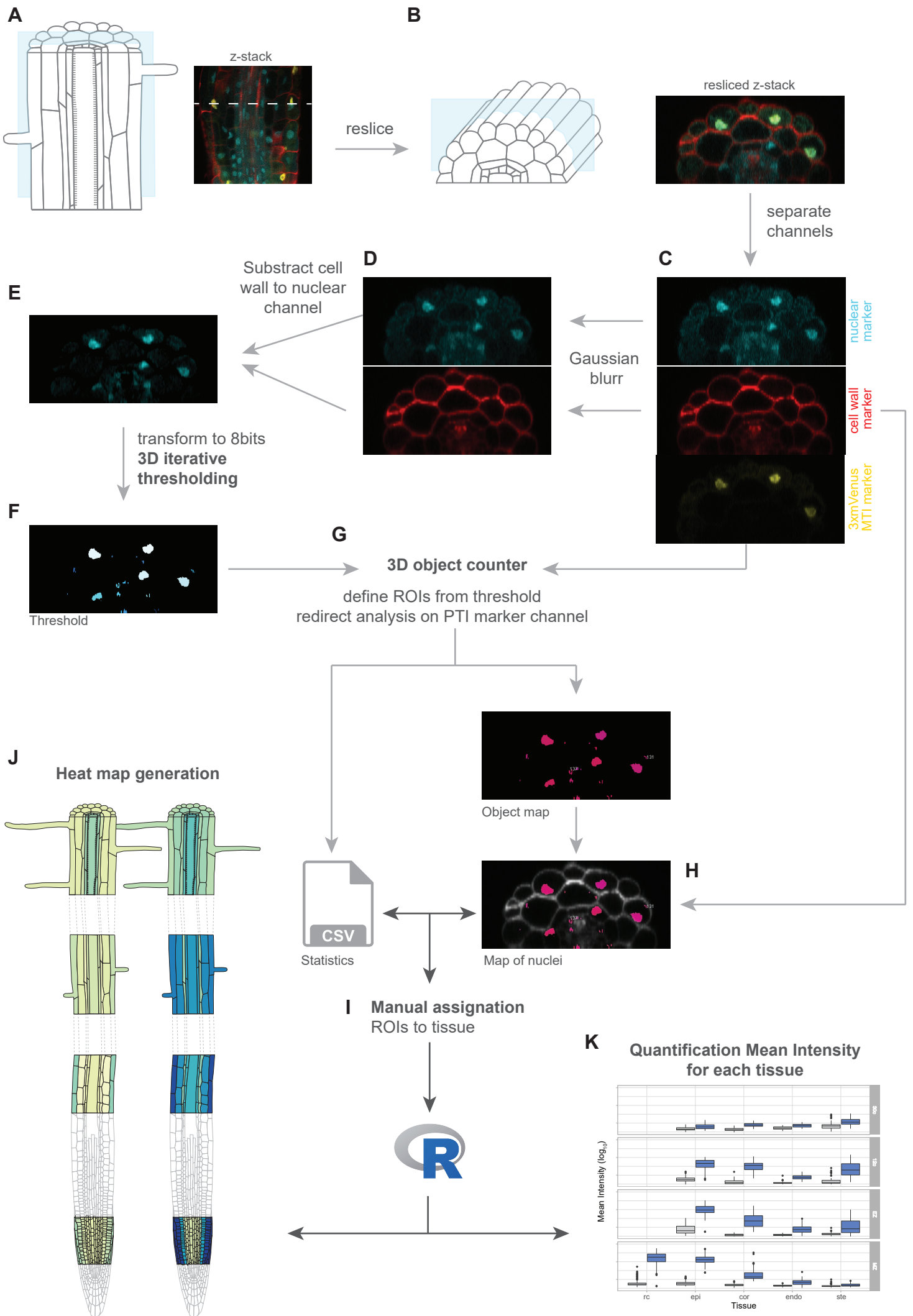


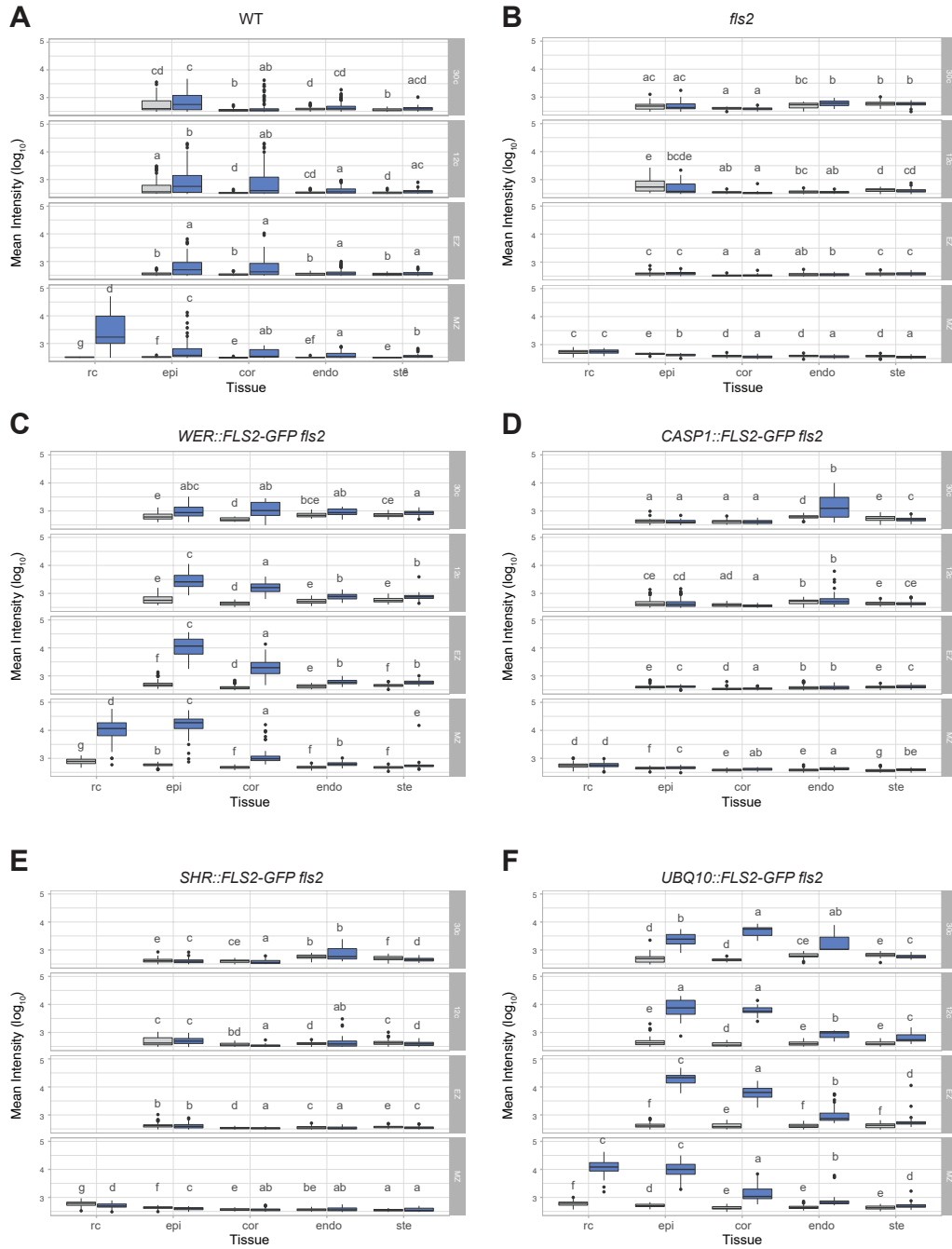
**Figure S2: Quantification procedure, related to Figure 2 and 3**

**(A)** Z-stack images with 3 channels (red: cell wall, blue: *UBQ10::NLS-mTurquoise/tdTomato*, yellow: *PER5/MYB51::NLS-3mVenus*) were taken from 4 different regions of the root (meristematic zone, elongation zone, 12 cells and 30 cells after onset of elongation), for 3-6 seedlings by treatment by genotype. **(B)** Each Z-stacks are resliced to get cross-section view. The three channels are separated **(C)** and a Gaussian blur filter is applied on the cell wall and the MAMP response marker channel **(D)**. Blurred cell wall channel is then subtracted from blurred nuclear marker channel to remove non-nuclear background **(E)**. The obtained cleaned nuclear channel is then converted to 8-bit and a 3D iterative thresholding is performed to delimit ROI for each nuclei **(F)**. The 3D object counter plugin is then used to measure the mean signal intensity of each nuclei delimited by the obtained ROIs in the MAMP RESPONSE marker channel. The plugin gives as output a .csv file with the measured values, a masked image of the PTI marker channel and an object map, delimiting the identified nuclei **(G)**. The object map is then coupled to the original cell wall marker to define the tissue origin of each nuclei **(H)**. Each map was then reviewed manually to assign 20 nuclei for each cell type and to complete .csv files **(I)**. Average of the mean signal intensity of each nuclear tissue-specific signal were calculated, transformed into  $\log_{10}$  and colour coded using the `heatmaply()` function in R **(J)**. Boxplots were generated to represent signal variability **(K)**.

Treatment



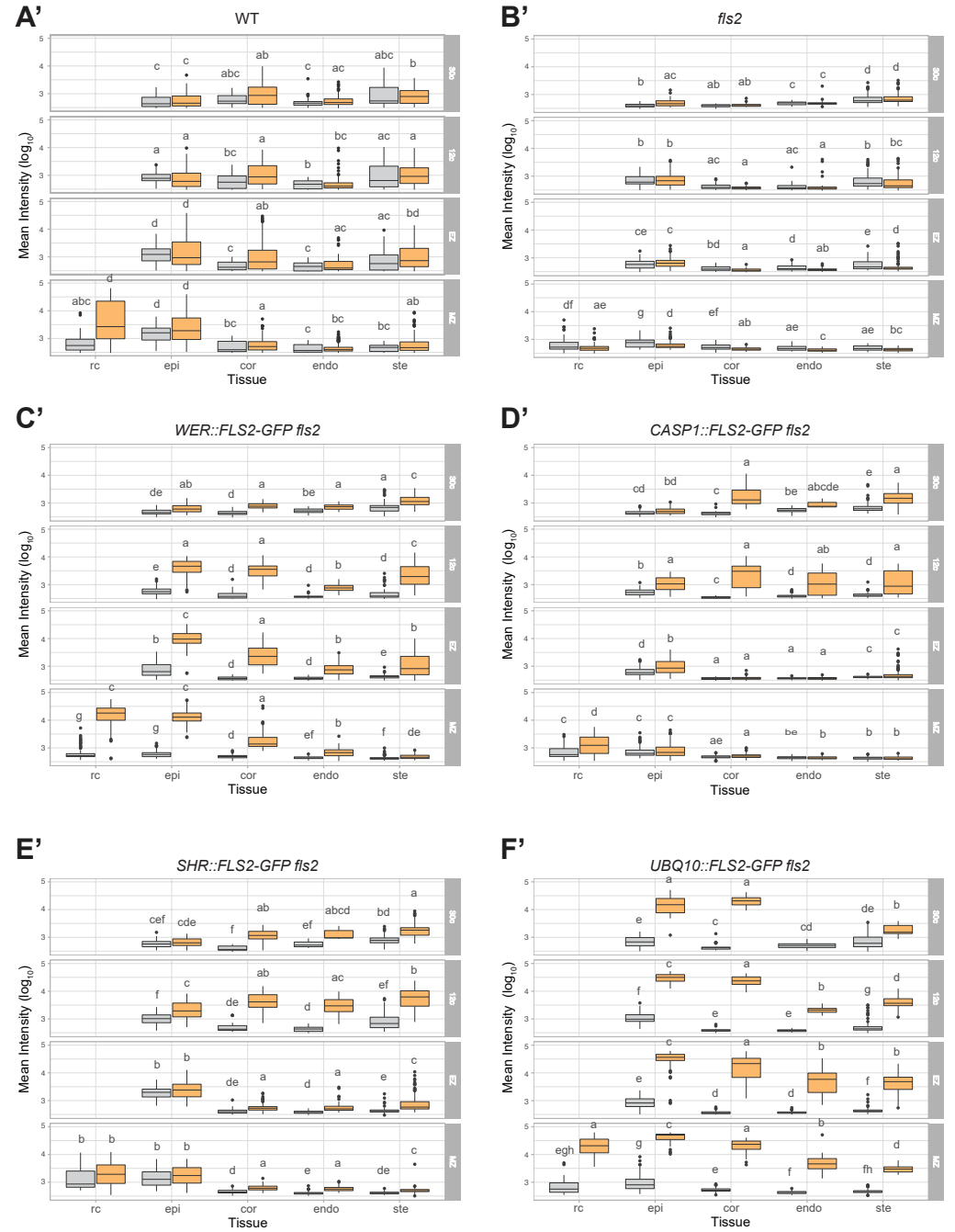
*PER5::NLS-3mV*  
*prom::FLS2-GFP fls2*



Treatment

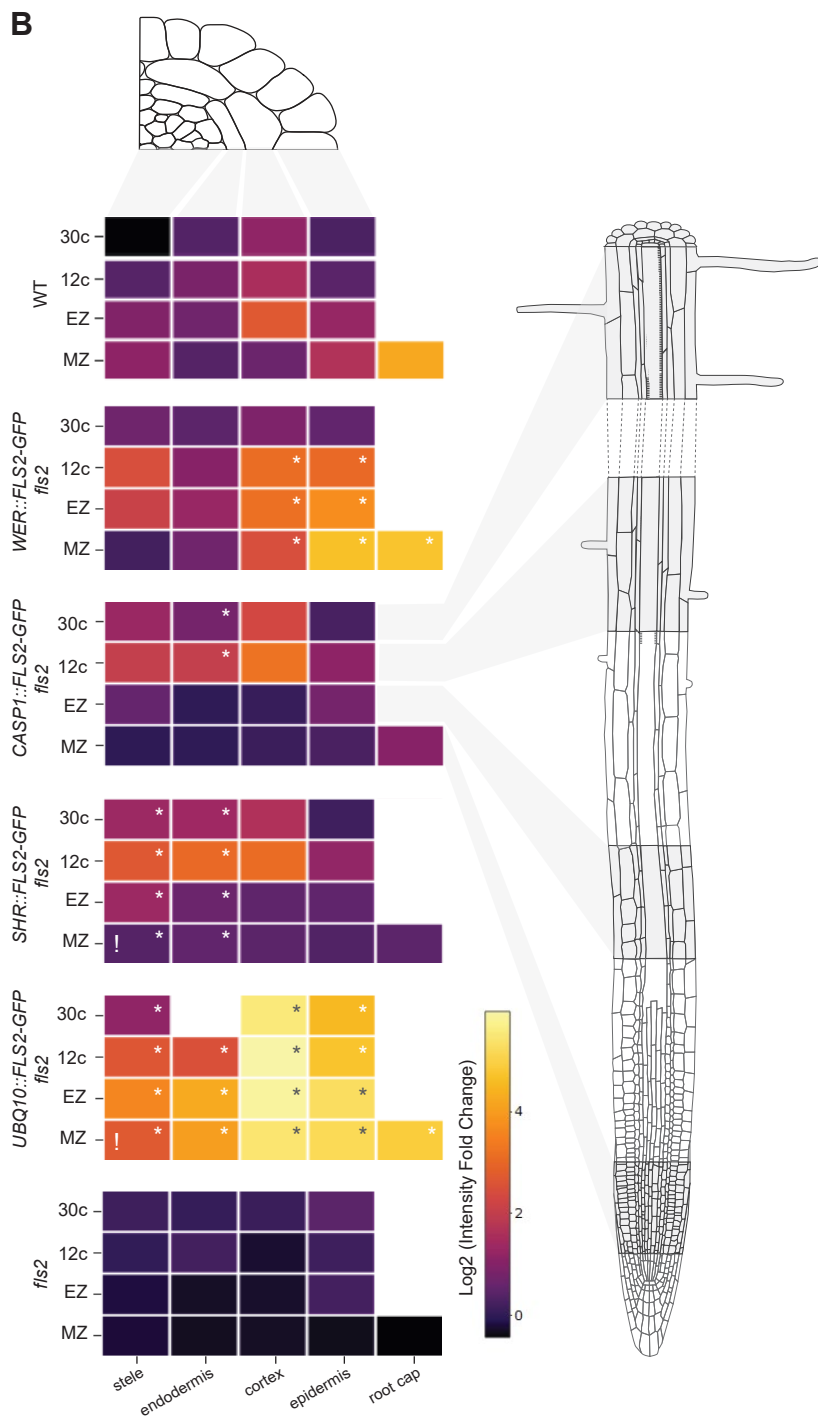
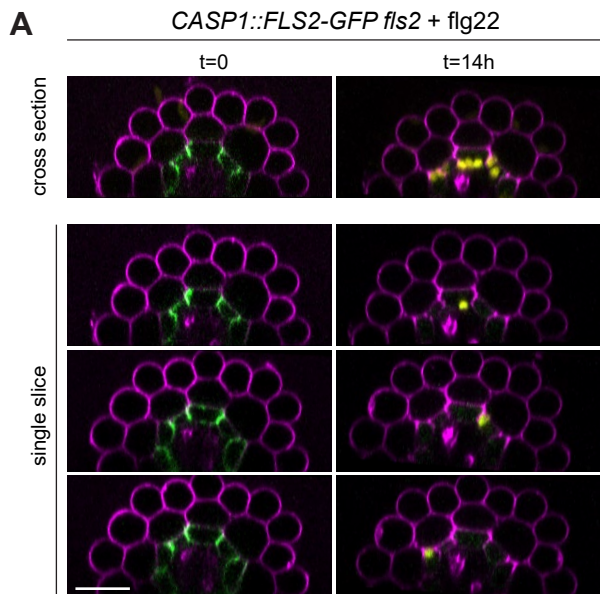


*MYB51::NLS-3mV*  
*prom::FLS2-GFP fls2*



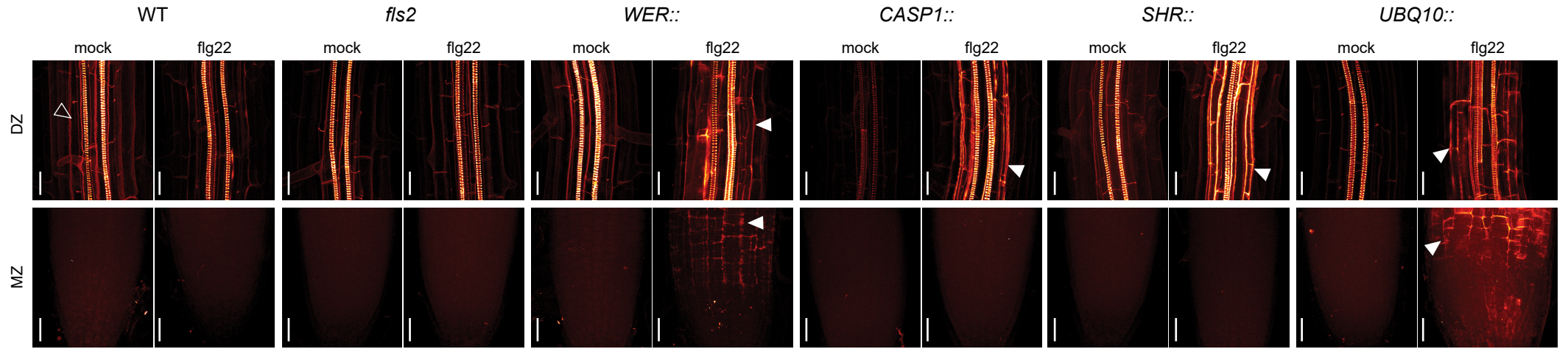
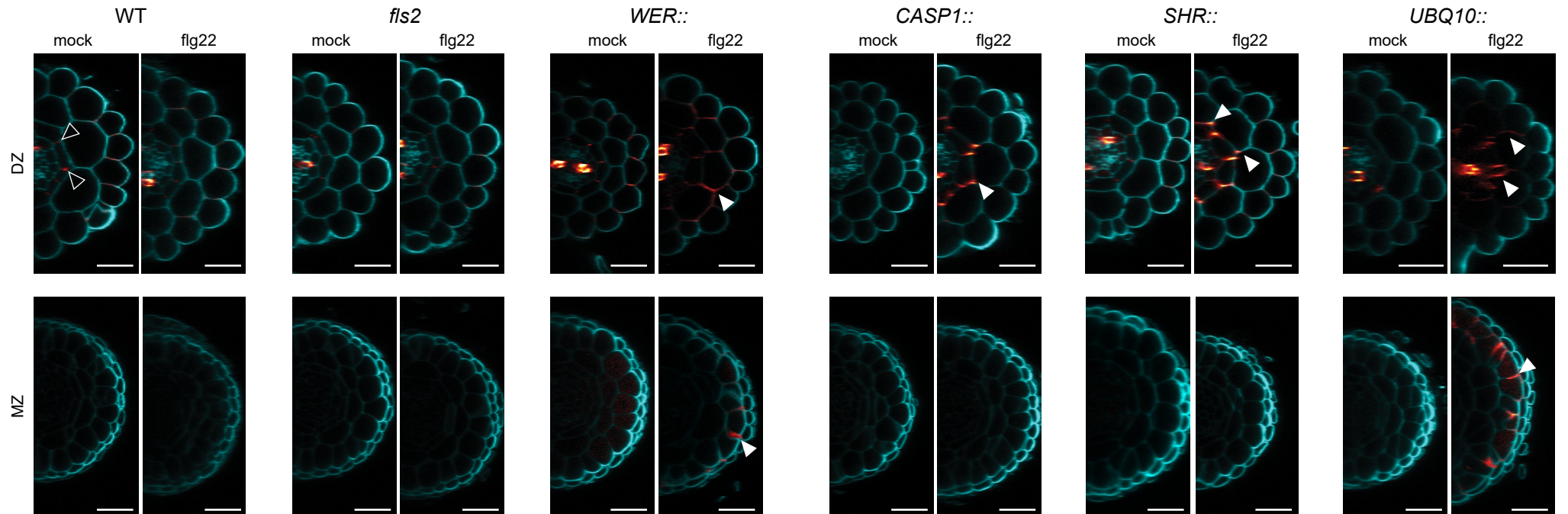
**Figure S3: *PER5* and *MYB51* tissue-specific quantification values, related to Figure 2 and 3**

Boxplots for mean intensity of *PER5::NLS-3mVenus* (A-F) and *MYB51::NLS-3mVenus* (A'-F') marker calculated from tissue-specific nuclear signals for (A) wild-type plants (Col-0), (B) *fls2* (SAIL691\_C04) mutant, (C) *WER::FLS2-GFP fls2*, (D) *CASP1::FLS2-GFP fls2*, (E) *SHR::FLS2-GFP fls2* and (F) *UBQ10::FLS2-GFP fls2*. Boxplot centre represents the median. (*PER5*: n = 16680, *MYB51*: n = 15180). Different letters indicate statistically significant differences ( $p < 0.001$  for all genotypes except for *CASP1::FLS2-GFP fls2* and *SHR::FLS2-GFP fls2* with *PER5::NLS-3mVenus*, where  $p < 0.05$ ) between means by Kruskal-Wallis and Pairwise Wilcoxon rank Sum tests for multiple comparison (p-values adjusted with Benjamini & Hochberg). MZ, meristematic zone; EZ, elongation zone; 15c, 15 cells after onset of elongation; 30c, 30 cells after onset of elongation; rc, root cap; epi, epidermis; cor, cortex; endo, endodermis; ste, stele.



**Figure S4: MYB51 and PER5 appear respectively non-cell autonomous and cell-autonomous responses, related to Figure 2 and 3.**

**(A)** Flg22 induces PER5 expression almost exclusively in the endodermis of *CASP1::FLS2-GFP fls2*. Picture taken at the same site before (t=0) and after (t = 14h) flg22 treatment. **(B)** Log<sub>2</sub> transformed fold change of intensity of *MYB51::NLS-3mVenus* in WT (Col-0), *fls2* (SAIL691\_C04) and the different *prom::FLS2-GFP fls2* lines for data presented in Figure S3. Pattern of induction of *MYB51* changed between the different lines but increased signal is not restricted to tissue expressing *FLS2* (stars). Note that *MYB51* can be induced in the stellar meristem in *UBQ10::FLS2* but not in *SHR::FLS2* (!). Three to six seedlings per genotype per treatment were analysed (n = 59, 15180 different nuclei analysed). MZ, meristematic zone; EZ, elongation zone; 15c, 15 cells after onset of elongation; 30c, 30 cells after onset of elongation; rc, root cap; epi, epidermis; cor, cortex; endo, endodermis; ste, stele.

**A***prom::FLS2-GFP fls2***B***prom::FLS2-GFP fls2*

**Figure S5: Lignin deposition is a cell-autonomous process, related to Figure 5**

**(A)** Maximum projection showing lignin deposition stained by basic fuchsin in the meristematic zone (MZ) and the differentiated zone (DZ) of the different *prom::FLS2-GFP fls2* lines after 1 day treatment with 1 $\mu$ M flg22. While neither wild-type (Col-0 background) nor *fls2* (SAIL691\_C04) roots show lignin deposition outside of the xylem and the endodermal Casparian strip barrier, *WER::* and *UBQ10::FLS2-GFP fls2* lines deposit lignin in both MZ and DZ. In contrast, *CASP1::* and *SHR::FLS2-GFP fls2* lignified heavily the DZ only. Black arrowheads, Casparian strip. White arrowheads, ectopic lignin deposition. Scale bar, 25 $\mu$ m. **(B)** Cross section of z-stack presented in (A). Cell wall stained with calcofluor (blue) is co-visualized with lignin stained with basic fuchsin (red). *WER::FLS2-GFP* expression drives lignin deposition between cortex and epidermal cells in DZ, and between epidermal cells and root cap in MZ. This pattern is also observed in *UBQ10::FLS2*, but extends to cortex and endodermis in DZ. Both *CASP1::* and *SHR::* deposit lignin ectopically between cortex and endodermal cells after flg22 treatment. Ten to 20 seedlings over 5 independent biological replicates were analysed for each genotype and treatment. White arrowheads, ectopic lignin. Black arrowheads, Casparian strip. Scale bar, 20 $\mu$ m.

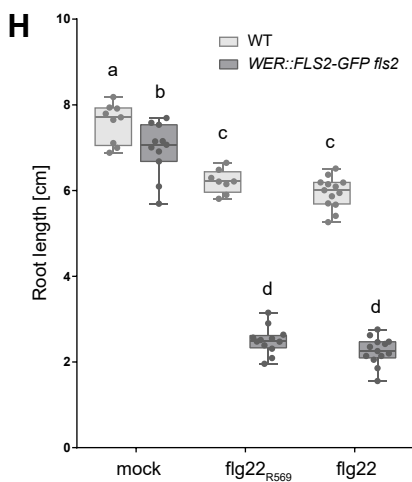
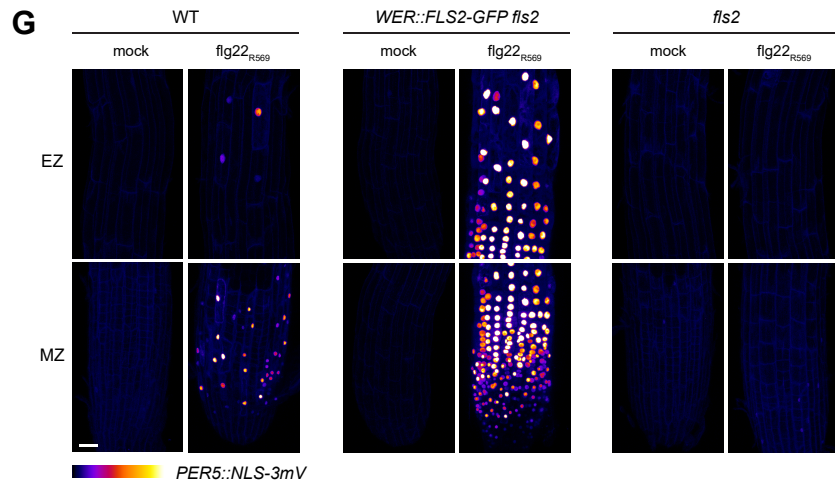
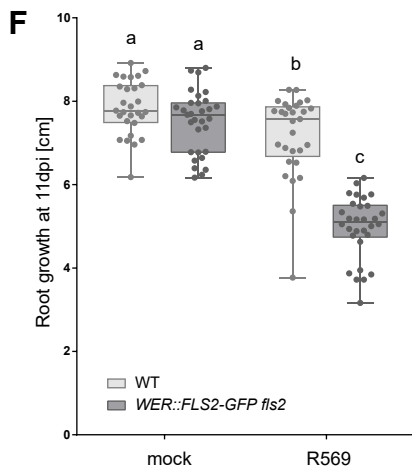
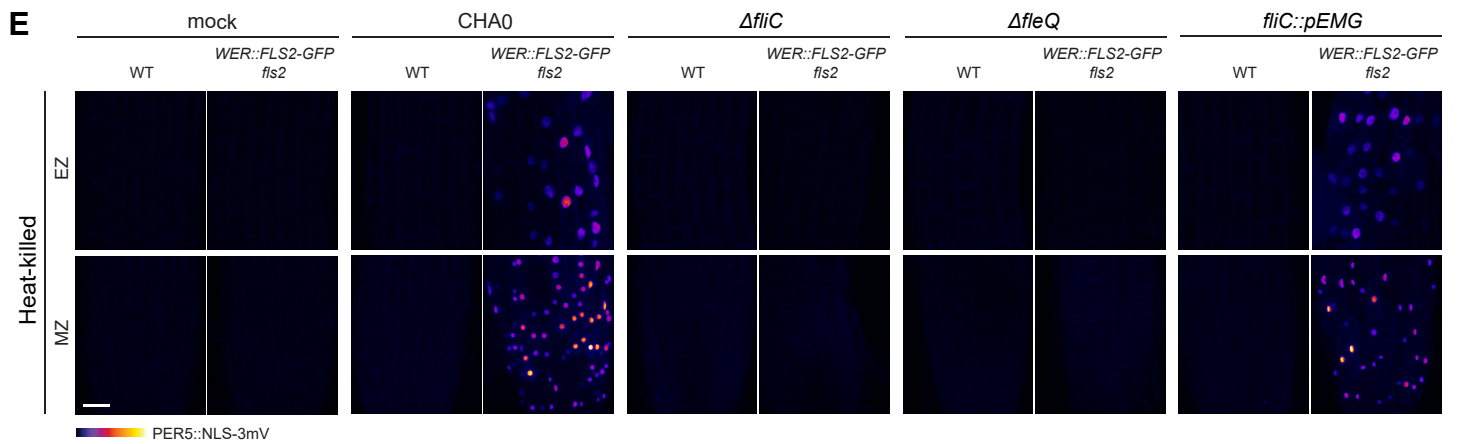
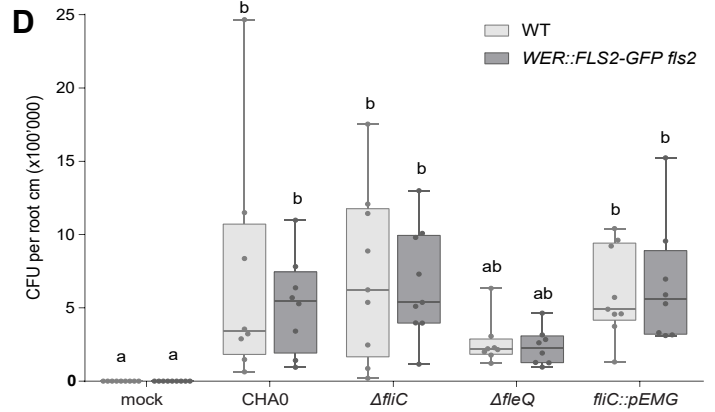
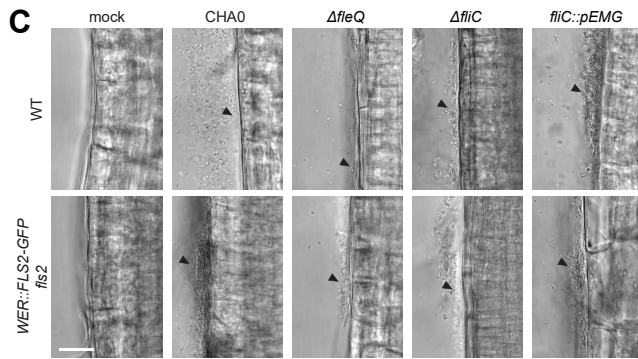
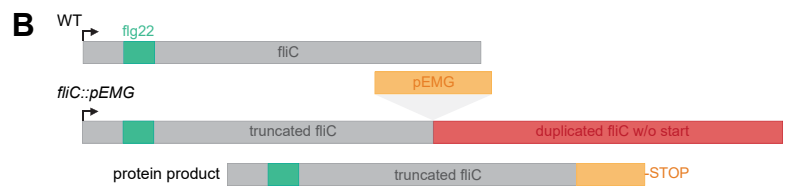
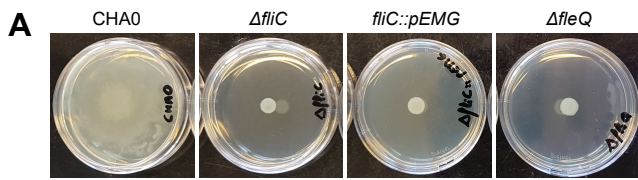


**Figure S6: Flg22 from bacterial isolate *Pseudomonas* R569 is recognized by *WER::FLS2*, related to Figure 7**

**(A)** Mutants  $\Delta fliC$ ,  $fliC::pEMG$  and  $\Delta fleQ$  are impaired in motility compared to CHA0 strain. **(B)** *fliC* mutation in the  $fliC::pEMG$  strain. The pEMG vector was inserted at the end of the *fliC* gene, truncating it. The *fliC* gene is duplicated from the middle of the flg22 sequence following the insertion. The non-functional protein predicted to be translated from the  $fliC::pEMG$  locus still possess a correct flg22 sequence. **(C)** Pictures of bacteria on root surface of WT and *WER::FLS2-GFP fls2*. All strains can colonize the root. Black arrowhead, bacteria. Scale bar, 20 $\mu$ m. **(D)** CFU counts per cm of root for WT (*PER5::NLS-3mVenus* in Col-0) and *WER::FLS2-GFP fls2* (*PER5::NLS-3mVenus* background) after treatment with CHA0,  $\Delta fliC$ ,  $\Delta fleQ$  and  $fliC::pEMG$  mutants. Four-day old seedlings were drop-inoculated with bacterial solution (OD<sub>600</sub> = 0.01) or mock, respectively. Three roots were collected and pooled for each sample. Data of three independent biological replicates were pooled (n = 9, total = 90). Different letters indicate statistically significant difference between means by Kruskal-Wallis test and Dunn's multiple comparison (p < 0.05). **(E)** Heat-killed CHA0 and  $fliC::pEMG$  mutant induce *PER5::NLS-3mVenus* expression (Fire LUT) in *WER::FLS2-GFP fls2* compared to WT (Col-0 background). Mutation in *fliC* and *fleQ* abolish the induction of PER5. Maximum projections of z-stacks imaging meristematic (MZ) and elongation (EZ) zones treated with drop inoculation of heat-killed bacterial solution of a concentration of OD<sub>600</sub> = 9 or mock, respectively. Representative images were acquired at 1 dpi (n = 12 on two replicates). Acquisition done with identical settings. Scale bar, 25 $\mu$ m. **(F)** Bacterial isolate R569 induces stronger root growth inhibition on *WER::FLS2-GFP fls2* than on wild-type seedlings (WT, Col-0 background). Replicate carried out in Cologne with different growth conditions (see material and methods). Five-days old seedlings were transferred for 11 days on plate containing bacteria at a concentration of OD<sub>600</sub> = 0.01. Boxplot centre represents the median. Different letters indicate statistically significant difference (p<0.05) between means by ANOVA and Tukey's multiple comparison tests. **(G)** flg22<sub>R569</sub> triggers a strong induction of *PER5::NLS-3mVenus* marker (Fire LUT) on *WER::FLS2-GFP fls2* compared to wild-type plant, but the detection is abolished in the *fls2* (SAIL691\_C04) mutant. Maximum projection of z-stacks imaging meristematic (MZ) and elongation (EZ) zones treated for 1 day with 1 $\mu$ M flg22<sub>R569</sub>. Acquisition done with identical settings. Representative images are shown (n = 10 on three replicates). Scale bar, 25 $\mu$ m. **(H)** flg22<sub>R569</sub> inhibits root growth weakly on wild-type (WT, Col-0 background) and strongly on *WER::FLS2-GFP fls2* in the same extent than commercial flg22 for *P. aeruginosa*. Seedlings were transferred for 7 days on plates containing 1 $\mu$ M flg22, flg22<sub>R569</sub> or mock. Boxplot centre represents the median. Different letters indicate statistically significant difference (p<0.05) between means by 2-ways ANOVA and Tukey's multiple comparison tests.

Number At- SPHERE	Phylum	Class	Order	Family	Genus
Root 1464	<i>Actinobacteria</i>	<i>Actinobacteria</i>	<i>Actinomycetales</i>	<i>Microbacteriaceae</i>	
Root 227	<i>Actinobacteria</i>	<i>Actinobacteria</i>	<i>Actinomycetales</i>	<i>Microbacteriaceae</i>	
Root 935	<i>Bacteroidetes</i>	<i>Flavobacteriia</i>	<i>Flavobacteriales</i>	<i>Flavobacteriaceae</i>	<i>Flavobacterium</i>
Root 444D2	<i>Firmicutes</i>	<i>Bacilli</i>	<i>Bacillales</i>	<i>Paenibacillaceae</i>	<i>Paenibacillus</i>
Root 342	<i>Proteobacteria</i>	<i>Alphaproteobacteria</i>	<i>Caulobacterales</i>	<i>Caulobacteraceae</i>	<i>Caulobacter</i>
Root 700	<i>Proteobacteria</i>	<i>Alphaproteobacteria</i>	<i>Caulobacterales</i>	<i>Caulobacteraceae</i>	
Root 105	<i>Proteobacteria</i>	<i>Alphaproteobacteria</i>	<i>Rhizobiales</i>	<i>Hyphomicrobiaceae</i>	
Root 1471	<i>Proteobacteria</i>	<i>Alphaproteobacteria</i>	<i>Rhizobiales</i>	<i>Phyllobacteriaceae</i>	
Root 482	<i>Proteobacteria</i>	<i>Alphaproteobacteria</i>	<i>Rhizobiales</i>	<i>Rhizobiaceae</i>	<i>Rhizobium</i>
Root 954	<i>Proteobacteria</i>	<i>Alphaproteobacteria</i>	<i>Rhizobiales</i>	<i>Rhizobiaceae</i>	<i>Rhizobium</i>
Root 142	<i>Proteobacteria</i>	<i>Alphaproteobacteria</i>	<i>Rhizobiales</i>	<i>Rhizobiaceae</i>	<i>Sinorhizobium</i>
Root 50	<i>Proteobacteria</i>	<i>Alphaproteobacteria</i>	<i>Sphingomonadales</i>	<i>Sphingomonadaceae</i>	<i>Sphingomonas</i>
Root 1294	<i>Proteobacteria</i>	<i>Alphaproteobacteria</i>	<i>Sphingomonadales</i>	<i>Sphingomonadaceae</i>	<i>Sphingomonas</i>
Root 710	<i>Proteobacteria</i>	<i>Alphaproteobacteria</i>	<i>Sphingomonadales</i>	<i>Sphingomonadaceae</i>	<i>Sphingomonas</i>
Root 241	<i>Proteobacteria</i>	<i>Alphaproteobacteria</i>	<i>Sphingomonadales</i>	<i>Sphingomonadaceae</i>	<i>Sphingomonas</i>
Root 1497	<i>Proteobacteria</i>	<i>Alphaproteobacteria</i>	<i>Sphingomonadales</i>	<i>Sphingomonadaceae</i>	<i>Sphingopyxis</i>
Root 214	<i>Proteobacteria</i>	<i>Alphaproteobacteria</i>	<i>Sphingomonadales</i>	<i>Sphingomonadaceae</i>	<i>Sphingopyxis</i>
Root 154	<i>Proteobacteria</i>	<i>Alphaproteobacteria</i>	<i>Sphingomonadales</i>	<i>Sphingomonadaceae</i>	
Root 83	<i>Proteobacteria</i>	<i>Betaproteobacteria</i>	<i>Burkholderiales</i>	<i>Alcaligenaceae</i>	<i>Achromobacter</i>
Root 170	<i>Proteobacteria</i>	<i>Betaproteobacteria</i>	<i>Burkholderiales</i>	<i>Alcaligenaceae</i>	<i>Achromobacter</i>
Root 565	<i>Proteobacteria</i>	<i>Betaproteobacteria</i>	<i>Burkholderiales</i>	<i>Alcaligenaceae</i>	<i>Achromobacter</i>
Root 473	<i>Proteobacteria</i>	<i>Betaproteobacteria</i>	<i>Burkholderiales</i>	<i>Comamonadaceae</i>	<i>Variovorax</i>
Root 568	<i>Proteobacteria</i>	<i>Betaproteobacteria</i>	<i>Burkholderiales</i>	<i>Comamonadaceae</i>	
Root 1221	<i>Proteobacteria</i>	<i>Betaproteobacteria</i>	<i>Burkholderiales</i>	<i>Comamonadaceae</i>	
Root 29	<i>Proteobacteria</i>	<i>Betaproteobacteria</i>	<i>Burkholderiales</i>	<i>Comamonadaceae</i>	
Root 16D2	<i>Proteobacteria</i>	<i>Betaproteobacteria</i>	<i>Burkholderiales</i>	<i>Comamonadaceae</i>	
Root 209	<i>Proteobacteria</i>	<i>Betaproteobacteria</i>	<i>Burkholderiales</i>	<i>Comamonadaceae</i>	
Root 401	<i>Proteobacteria</i>	<i>Gammaproteobacteria</i>	<i>Pseudomonadales</i>	<i>Pseudomonadaceae</i>	<i>Pseudomonas</i>
Root 562	<i>Proteobacteria</i>	<i>Gammaproteobacteria</i>	<i>Pseudomonadales</i>	<i>Pseudomonadaceae</i>	<i>Pseudomonas</i>
Root 9	<i>Proteobacteria</i>	<i>Gammaproteobacteria</i>	<i>Pseudomonadales</i>	<i>Pseudomonadaceae</i>	<i>Pseudomonas</i>
Root 569	<i>Proteobacteria</i>	<i>Gammaproteobacteria</i>	<i>Pseudomonadales</i>	<i>Pseudomonadaceae</i>	<i>Pseudomonas</i>
Root 68	<i>Proteobacteria</i>	<i>Gammaproteobacteria</i>	<i>Pseudomonadales</i>	<i>Pseudomonadaceae</i>	<i>Pseudomonas</i>
Root 71	<i>Proteobacteria</i>	<i>Gammaproteobacteria</i>	<i>Pseudomonadales</i>	<i>Pseudomonadaceae</i>	<i>Pseudomonas</i>
Root 179	<i>Proteobacteria</i>	<i>Gammaproteobacteria</i>	<i>Xanthomonadales</i>	<i>Xanthomonadaceae</i>	<i>Rhodanobacter</i>

Table S1: Bacteria taxonomy, related to Figure 7

Number	Family	Genus	Presence of <i>fliC</i> gene	% identity to <i>fliC</i> from CHA0	Query score	flg22 predicted <sup>3</sup>	MAMP RESPONSE WER>WT	RGI WER>WT
Root 1464	Microbacteriaceae		no	-	-	no	no	no
Root 227	Microbacteriaceae		yes	43.31%	100%	no	no/yes	no
Root 935	Flavobacteriaceae	<i>Flavobacterium</i>	no	-	-	no	no	no
Root 444D2	Paenibacillaceae	<i>Paenibacillus</i>	yes	35.44%	99%	no	yes	no
Root 342	Caulobacteraceae	<i>Caulobacter</i>	yes	25.96%	100%	no	- <sup>a</sup>	no
Root 700	Caulobacteraceae		yes	24.03%	100%	no	-	no
Root 105	Hyphomicrobiaceae		no	-	-	no	-	no
Root 1471	Phyllobacteriaceae		no	-	-	no	- <sup>a</sup>	no
Root 482	Rhizobiaceae	<i>Rhizobium</i>	yes	25%	55%	no	no	no
Root 954	Rhizobiaceae	<i>Rhizobium</i>	yes	26.8%	32%	no	no	no
Root 142	Rhizobiaceae	<i>Sinorhizobium</i>	yes	23.19%	79%	no	no	no
Root 50	Sphingomonadaceae	<i>Sphingomonas</i>	yes	44.33%	98%	yes	no	no
Root 1294	Sphingomonadaceae	<i>Sphingomonas</i>	yes	44.33%	98%	yes	no	no
Root 710	Sphingomonadaceae	<i>Sphingomonas</i>	yes	40.91%	98%	yes	no	no
Root 241	Sphingomonadaceae	<i>Sphingomonas</i>	yes	42.91% / 23.08%	98% / 100%	yes	no/yes <sup>b</sup>	no
Root 1497	Sphingomonadaceae	<i>Sphingopyxis</i>	yes	42.29%	98%	yes	no	no
Root 214	Sphingomonadaceae	<i>Sphingopyxis</i>	yes	39.5%	98%	yes	yes	no/yes
Root 154	Sphingomonadaceae		yes	39.5%	98%	yes	yes	no/yes
Root 83	Alcaligenaceae	<i>Achromobacter</i>	yes	46.99%	100%	yes	no	no
Root 170	Alcaligenaceae	<i>Achromobacter</i>	yes	46.45%	100%	yes	yes	no/yes
Root 565	Alcaligenaceae	<i>Achromobacter</i>	yes	46.45%	99%	yes	yes <sup>b</sup>	no
Root 473	Comamonadaceae	<i>Variovorax</i>	yes	49.18%	99%	yes	no	no
Root 568	Comamonadaceae		yes	61.18% / 53.1%	97% / 100%	no	no	no
Root 1221	Comamonadaceae		yes	47.18%	100%	yes	no/yes	no
Root 29	Comamonadaceae		yes	52.11%	100%	yes	no	no
Root 16D2	Comamonadaceae		yes	52.11%	100%	yes	no/yes	no
Root 209	Comamonadaceae		yes	57.59%	98	yes	yes	no
Root 401	Pseudomonadaceae	<i>Pseudomonas</i>	yes	66.45%	95%	no	no	no
Root 562	Pseudomonadaceae	<i>Pseudomonas</i>	yes	65.84%	92%	no	yes	no
Root 9	Pseudomonadaceae	<i>Pseudomonas</i>	yes	70.39%	84%	no	yes	yes
Root 569	Pseudomonadaceae	<i>Pseudomonas</i>	yes	63.16%	100%	no	yes	yes
Root 68	Pseudomonadaceae	<i>Pseudomonas</i>	yes	70.67%	100%	yes	yes	no
Root 71	Pseudomonadaceae	<i>Pseudomonas</i>	yes	70.67%	100%	yes	yes	no
Root 179	Xanthomonadaceae	<i>Rhodanobacter</i>	no	-	-	no	no <sup>b</sup>	no

No/yes refers to variable and opposite results across replicates

<sup>a</sup> not tested: bacteria did not grow in drop inoculation experiment

<sup>b</sup> induction of *PER5* in differentiated zone for both WT and *WER::FLS2-GFP fls2*

<sup>c</sup> prediction published<sup>51</sup>

**Table S2: Summary of bacteria screen for PTI assay and RGI assay, related to Figure 7**

Name	Sequence / plasmid characteristics <sup>a</sup>	Reference
<b>Primers</b>		
fleQ-1	CGGGATCCATTGAAGAAACCCGTGAGGC	[S2]
fleQ-2	CCCAAGCTTTAAAATCACCGCCAGGTCGCG	[S2]
fleQ-3	CCCAAGCTTTGACGCCGGTTTTCAAGTCTTTG	[S2]
fleQ-4	GGAATTCATTTTCATGGCCATCGTCTTCGCG	[S2]
fliC-1	ATAACAGGGTAATCTGAATTATGAATCAGCTAGAGCCTGT	this study
fliC-2	CCAGCTATTACATGACGAATTCCTCGTTG	this study
fliC-3	ATTCGTCATGTAATAGCTGGCTAAGCTTTGGC	this study
fliC-4	CCGGGTACCGAGCTCGAATTTAGGCCTTGGCACT	this study
fliC_check_F	GACTTCGCAGATCCGTGG	this study
fliC_check_R	AACTGCGGTCTGAAGCTTG	this study
fliC-pEMG-1	CGGGATCCTGAAGATCAACAGCGCAAAG	[S2]
fliC-pEMG-2	GGAATTCAGCAGCGAAGTCGGTATCT	[S2]
<b>Plasmids</b>		
pEMG	Expression vector; <i>oriR6K</i> , <i>lacZα</i> with two flanking I-SceI sites; Km <sup>R</sup> , Ap <sup>R</sup>	[S3]
pSW-2	<i>oriRK2</i> , <i>xyIS</i> , <i>P<sub>m</sub>::I-sceI</i> ; Gm <sup>R</sup>	[S3]
pME8323	pEMG::Δ <i>fleQ</i> ; suicide plasmid for the in-frame deletion of <i>fleQ</i> (PPRCHA0_1656)	[S2]
pME11121	pEMG::Δ <i>fliC</i> ; suicide plasmid for the in-frame deletion of <i>fliC</i> (PPRCHA0_1651)	this study

<sup>a</sup>: Gm<sup>r</sup>, gentamicin resistance; Km<sup>r</sup>, kanamycin resistance.

**Table S3: Primers and plasmids used for bacterial mutagenesis, related to STAR Methods**

## Supplemental References

- S1. Garrido-Oter, R., Nakano, R.T., Dombrowski, N., Ma, K.-W., McHardy, A.C., and Schulze-Lefert, P. (2018). Modular Traits of the Rhizobiales Root Microbiota and Their Evolutionary Relationship with Symbiotic Rhizobia. *Cell Host & Microbe* 24, 155-167.e5.
- S2. Kupferschmied, P. (2015). Molecular basis and regulation of insect pathogenicity in plant-beneficial pseudomonads. Available at: [https://serval.unil.ch/notice/serval:BIB\\_FB118BB07158](https://serval.unil.ch/notice/serval:BIB_FB118BB07158) [Accessed March 31, 2020].
- S3. Martínez-García, E., and Lorenzo, V. de (2011). Engineering multiple genomic deletions in Gram-negative bacteria: analysis of the multi-resistant antibiotic profile of *Pseudomonas putida* KT2440. *Environmental Microbiology* 13, 2702–2716.